Wind Energ. Sci. Discuss., doi:10.5194/wes-2016-53, 2016
Manuscript under review for journal Wind Energ. Sci.
Published: 23 December 2016

eawe european academy of wind energy
Open Access WIND ENERGY SCIENCE DISCUSSIONS

Aeroelastic Stability of Idling Wind Turbines

Kai Wang[1], Vasilis A. Riziotis[2], Spyros G. Voutsinas[2]

[1] China-EU Institute for Clean and Renewable Energy, Huazhong University of Science and Technology, 1037 Luoyu Rd, Wuhan, China
[2] School of Mechanical Engineering, National Technical University of Athens, GR15780 Athens, Greece

Correspondence to: Vasilis A. Riziotis (vasilis@fluid.mech.ntua.gr)

Abstract. Wind turbine rotors in idling operation mode can experience high angles of attack, within the post stall region that are capable of triggering stall-induced vibrations. In the present paper, rotor stability in slow idling operation is assessed on the basis of non-linear time domain and linear eigenvalue analyses. Analysis is performed for a 10 MW conceptual wind turbine designed by DTU. First, the flow conditions that are likely to favour stall induced instabilities are identified through non-linear time domain aeroelastic simulations. Next, for the above specified conditions, eigenvalue stability simulations are performed aiming at identifying the low damped modes of the turbine. The eigenvalue stability results are evaluated through computations of the work of the aerodynamic forces under imposed harmonic motion following the shape and frequency of the various modes. Eigenvalue analysis indicates that the asymmetric and symmetric out-of-plane modes have the lowest damping. The results of the eigenvalue analysis agree well with those of the non-linear work analysis and the time domain analysis.

1 Introduction

In idling mode, the angles of attack (AOA) experienced by the blades significantly vary over one revolution under the combined effect of inflow turbulence, flow inclination and nacelle tilt and yaw. The variation of the AOAs remains substantial even in small yaw misalignments within the range of +/-15^o. It is noted that yaw errors in the above range are considered as normal idling conditions by wind turbine manufactures. Going to moderate yaw angles, the variations of the AOA can be such that the rotor enters stall both at positive and negative AOAs and thereby stall induced vibrations are likely to occur. In the past a lot of research effort has been directed to the analysis of stall induced vibrations (SIV) in normal operation, (Petersen et al, 1998; Hansen, 2003; Riziotis et al, 2004; Hansen, 2007), however very little has been done for parked or idling rotors.

Aeroelastic analysis of parked or idling rotors largely relies on blade element aerodynamic models. BEM models comply with industry's needs for fast aerodynamic tools, capable of performing certification simulations. In the context of blade element models, Politis et al (2009) investigated the stability characteristics of an isolated parked blade at various inflow angles using an eigenvalue approach and considering both steady-state but also unsteady aerodynamics. The paper focused on stall induced instabilities. It was shown that such instabilities can take place at inflow angles that slightly exceed C_{Lmax}

Wind Energ. Sci. Discuss., doi:10.5194/wes-2016-53, 2016
Manuscript under review for journal Wind Energ. Sci.
Published: 23 December 2016

eawe european academy of wind energy
Open Access WIND ENERGY SCIENCE DISCUSSIONS

AOA but also in the vicinity of +/-90^o AOA. In a similar context Skrzypiński & Gaunaa (2015) investigated the stability of an elastically mounted 2D section of the parked blade using engineering aerodynamic models. In their work, they investigated the effect of imposing temporal lag on the steady-state aerodynamic loads at very high AOA by using indicial functions. Despite the fact that the choice of the lag response was not based on measured information - a rather intuitive tuning of the model parameters has been performed - it was shown that in all cases an increase in the damping of the low damped edgewise modes is finally obtained even for very small delay values. In their work the authors have also investigated the effect of various structural parameters on the damping characteristics of a parked blade. Very recently Pirrung et al (2016) proposed a new hybrid model for the analysis of parked/idling rotors. The model is based on the coupling of a trailed vortex near wake model with a momentum type far wake model. In their work the authors have only presented time domain aerodynamic analysis results. However, the formulated model is linearizable and therefore can serve for eigenvalue aeroelastic stability analyses.

Although CFD models are still computationally expensive, especially in view of performing detailed time domain certification simulations, some work has been done at the level of advanced aerodynamic models. Skrzypiński et al (2014a) investigated stall induced vibrations using 2D RANS and 3D DES aerodynamic simulations for a typical elastically mounted blade section in combined flap-edge motion. The 3D simulations considered an extruded section and periodic spanwise flow conditions. The analysis focused on AOA that slightly exceed C_{Lmax}. It was concluded that the differences in the predicted post stall characteristics and the stability limits between 2D and 3D CFD analysis are significant. Skrzypiński et al (2014b) also investigated vortex shedding phenomena occurring at very high AOA, in the vicinity of 90^o using CFD models. Also in this work a typical elastically mounted blade section was considered. AOA of about 90^o can be encountered by a wind turbine blade during the installation phase or in case of a yaw system failure. Under such flow conditions vortex shedding phenomena can be combined with negative slopes of the lift curve that favour combined stall and vortex induced vibrations (VIV). Typical section analysis showed that lock-on at the vortex shedding frequency is likely to occur depending on the amplitude of the lead-lag motion undergone by the section. Finally, Heinz et al (2016) analysed the full blade configuration at 90^o AOA using a DES aerodynamic model coupled to a non-linear beam model of the blade. The analyses showed that at certain azimuth positions of the parked blade when the inflow has a significant velocity component along the blade axis, spanwise correlated vortex shedding over large parts of the blade can be triggered which eventually leads to excessive VIV.

Vortex shedding phenomena and VIV have been also investigated by Zou et al (2014) with vortex modeling. Massive flow separation over the blade surface was simulated in the context of the “double wake” concept. The “double wake” concept is based on the modelling principle that the flow separation bubble can be simulated by two vortex sheets one originating from the trailing edge of the blade and the other from the position where separation of the flow takes place. The work focused on a typical, elastically mounted blade section at high AOA and showed that VIV and lock-on phenomena are likely to occur at lower wind speeds while at higher wind speeds edgewise instabilities are mainly driven by the negative slope of the lift curve at AOA in the vicinity of 90^o. An important result of this work which confirms the findings of Skrzypiński & Gaunaa (2015), is that the unsteady character of the flow (temporal lag) increases the damping of the low

Wind Energ. Sci. Discuss., doi:10.5194/wes-2016-53, 2016
Manuscript under review for journal Wind Energ. Sci.
Published: 23 December 2016

damped edgewise modes at very high AOA and by that indicates that steady-state analysis is expected to be conservative.

In the present paper the stability behaviour of the conceptual 10 MW reference wind turbine (3 bladed, pitch regulated-variable speed turbine with diameter D=178.3 m) of the INNWIND.EU project (Bak et al, 2013) in slow idling operation is assessed using the linear eigenvalue stability tool GAST_lin (Riziotis et al, 2004). The objectives of the work are to first identify idling situations at moderate yaw misalignment angles, that favour stall induced vibrations and subsequently predict which of the turbine modes exhibit the lowest damping characteristics. The analysis is confined to yaw angles within the range [-60^o, +60^o]. This is the absolute upper limit up to which engineering dynamic stall models can be trusted. Outside this range deep stall conditions are encountered that cannot be properly addressed by engineering aerodynamic models. This is because engineering models lack the appropriate tuning in such deep stall conditions. Furthermore, in deep stall, vortex shedding phenomena take place that lead to additional periodic excitation of the rotor not included in the present engineering modeling framework.

The eigenvalue analysis results are compared against results of non linear time domain analysis as well as with results of aerodynamic work computations coming from forced harmonic oscillation simulations in which the imposed motion follows the shape and the frequency of the turbine modes. This is done in an attempt to prove that fast linear eigenvalue stability tools that have been widely employed by the industry for damping characterization in normal operation conditions can be also trusted for predicting damping in idling operation conditions.

The inflow conditions that favour stall induced instabilities are identified through turbulent wind non-linear time domain aeroelastic simulations at yaw angles in the range [-60^o, +60^o] (moderate to high yaw angles) using the hGAST aeroelastic modeling platform (Manolas et al, 2015). As already mentioned the above range of yaw angles defines the validated envelope of engineering dynamic stall models. Rotor azimuth positions and corresponding sectional AOAs at which instabilities are favoured are assessed. Moreover, the average rotor speeds for the different yaw angles are recorded in order to be used as input to the linear eigenvalue stability tool.

Based on the findings of the above time domain analysis, eigenvalue stability simulations are performed focusing on the conditions for which maximum edgewise loads are obtained with hGAST code. Stability analysis in the case of yaw misalignment requires application of Floquet's theory (Skjoldan & Hansen, 2009; Bottasso & Cacciola, 2015). Due to the essentially periodic character of the resulting dynamic system, Coleman's multi-blade transformation can no longer reduce the system to a constant coefficient one. Besides the anyway high cost of Floquet analysis, in idling conditions the rotational speed attains very low values that become at least ten times smaller than the lowest natural frequency of the turbine which further increases the cost to a prohibitive level for the here intended analysis. By noting that at very small rotational speeds (~1 RPM) low order harmonics (up to 6p) are not expected to interact strongly with the natural frequencies of the turbine, as an alternative, non-rotating (static) analysis can be performed at different azimuth angles within the sector [0^o, 120^o]. In order to approximate as closely as possible the rotating case a free-free drive train (free rotation boundary condition over the generator side) is simulated and the idling rotational speed (obtained through time domain simulations) is taken into account in formulating the local to the blade section velocity triangle.

Wind Energ. Sci. Discuss., doi:10.5194/wes-2016-53, 2016
Manuscript under review for journal Wind Energ. Sci.
Published: 23 December 2016

eawe european academy of wind energy
Open Access WIND ENERGY SCIENCE DISCUSSIONS

Finally, using as input the aeroelastic mode shapes and frequencies calculated through the eigenvalue analysis, aerodynamic work computations are performed. The turbine is set to a prescribed small amplitude harmonic motion following the shape and frequency of the various aeroelastic modes. The work done by the aerodynamic loads acting on the blades as a result of this forced vibration, is computed within one oscillation cycle. This work is directly related to the damping of the corresponding mode (Petersen et al, 1998). Non-linear work computations are compared to eigenvalue analysis results.

The results of the analysis indicated that the asymmetric and symmetric out-of-plane modes exhibit the lowest damping values. Among them, the asymmetric edge horizontal/tilt mode obtains negative damping values at the yaw angle of 30^o. The results of the eigenvalue analysis agree well with the results of the time domain analysis.

2 Background on the dynamics and aerodynamic loading of an idling turbine

In the present section some important features related to the dynamics and aerodynamics of an idling turbine are discussed. This background information is regarded essential to render stability results presented in the following sections intelligible.

Figure 1 presents the variation of the natural frequencies of the idling Reference 10 MW wind turbine versus pitch angle as it increases from 0^o to 90^o (towards feather). This plot is typically very similar for any three bladed turbine of similar design philosophy. As expected, the two first tower modes M1 and M2 are not affected at all by the change in the pitch angle. The frequencies of the first asymmetric flap modes M3 and M4 slightly increase while the frequencies of the first asymmetric edgewise modes M6 and M7 significantly decrease as the pitch angle increases. As a result, asymmetric flapwise and edgewise modes come closer in frequency to each other, despite their initial distinct separation at 0^o pitch angle. Bringing the asymmetric flap and edge modes closer will render the cross coupling between the corresponding bending directions stronger when the blades are in feather position. The frequency of the first symmetric out of plane mode M5 will gradually increase and finally at high pitch angles will exceed the frequency of the asymmetric edgewise modes M6 and M7. The frequency of the first symmetric in-plane (drive train) mode M8 decreases with the pitch angle and as the pitch tends to 90^o the frequency of M8 tends to coincide with the frequency of the symmetric out of plane mode M5. The second asymmetric flapwise modes M9 and M10 exhibit a similar behaviour with the first asymmetric flapwise modes M3 and M4.

Wind Energ. Sci. Discuss., doi:10.5194/wes-2016-53, 2016
Manuscript under review for journal Wind Energ. Sci.
Published: 23 December 2016

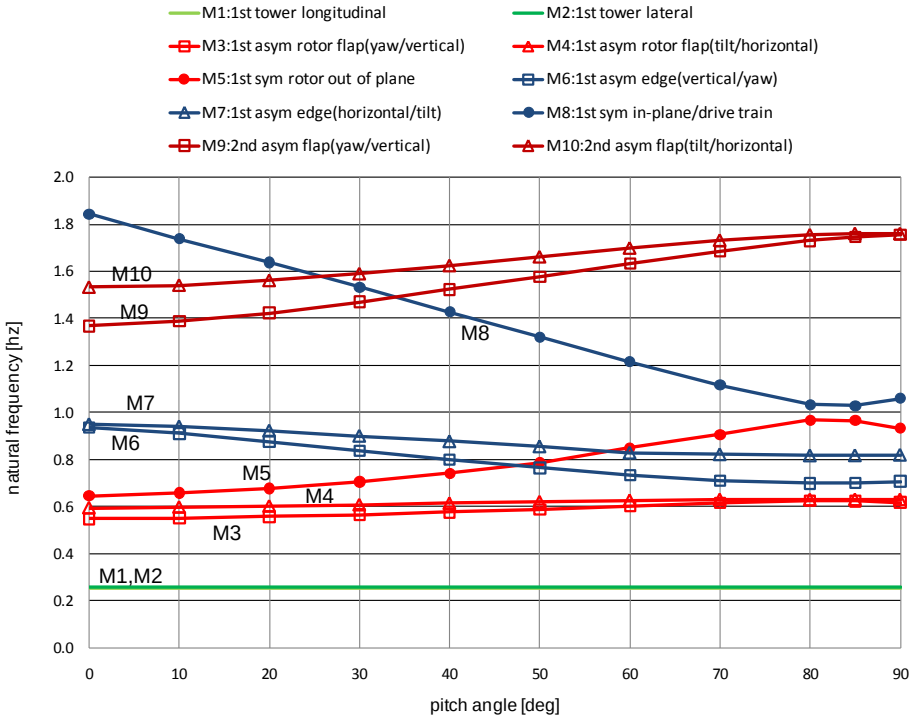

Figure 1. Natural frequencies of the 10 MW Reference Wind Turbine vs. pitch from 0° to 90° (towards feather).

As the blade pitches to feather, the asymmetric flapwise modes switch from out-of-plane to in-plane. Inversely the asymmetric edgewise modes switch from in-plane to out-of-plane. So, as the blade pitch changes from 0° to 90° the first asymmetric edgewise (in-plane) vertical mode M6 turns into a first asymmetric edgewise (out-of-pane) yawing mode and the first asymmetric edgewise (in-plane) horizontal mode M7 turns into a first asymmetric edgewise (out-of-pane) tilting mode. This transformation of the asymmetric edgewise modes is depicted in Figure 2(a) and (b). Inversely the first asymmetric flapwise (out-of-plane) yawing mode M3 turns into a first asymmetric flapwise (in-plane) vertical mode and the first asymmetric flapwise (out-of-plane) tilting mode M4 turns into a first asymmetric flapwise (in-plane) horizontal mode. Similar transformations are obtained in the second flapwise modes M9 and M10.

On the other hand the symmetric modes seem to retain their original character. So, as shown in Figure 3 the out-of-plane (flapwise) collective mode (M5) remains a collective out-of-plane (edgewise) mode as the pitch changes from 0° to 90°. At 0° pitch the coupling with the in-plane direction in M5 is negligible. At 90°, as the frequency of M5 gets close to the frequency of the collective in-plane M8 mode a coupling with the in-plane direction is established.

Wind Energ. Sci. Discuss., doi:10.5194/wes-2016-53, 2016
Manuscript under review for journal Wind Energ. Sci.
Published: 23 December 2016

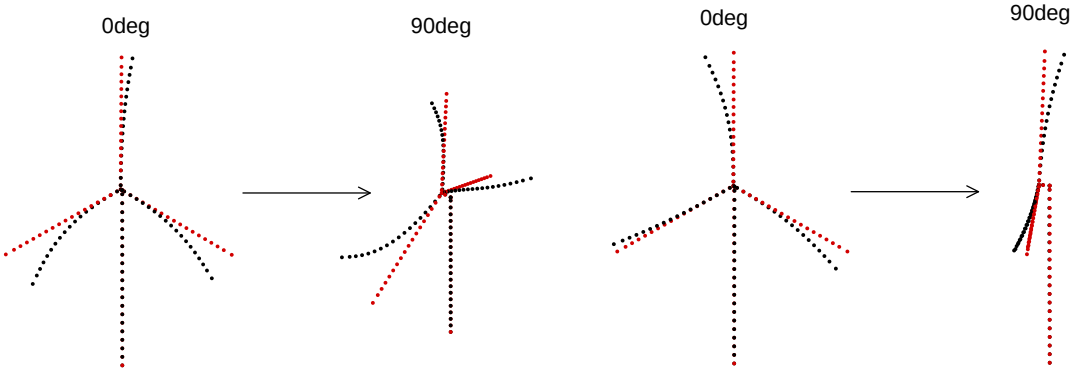

Figure 2. Mode shape alternation from 0° to 90° pitch for asymmetric edgewise modes (a) M6 and (b) M7. Red symbols: undeformed state, Black symbols: deformed state.

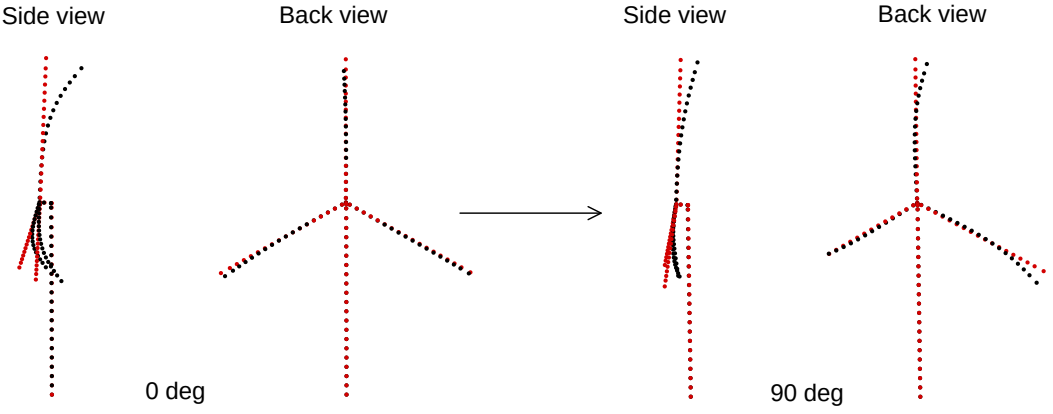

Figure 3. Mode shape alternation from 0° to 90° pitch for symmetric out-of-plane mode M5. Red symbols: undeformed state, Black symbols: deformed state.

Also as shown in Figure 4 the in-plane (edgewise) collective mode M8 remains a collective in-plane (flapwise) mode as the pitch changes from 0° to 90°. Originally, at 0° pitch a coupling with the second flapwise modes is clearly noted in the shape of the mode driven by the fact that the collective in-plane mode lies closely to the second flapwise asymmetric modes. At 90° pitch, as the frequency of the mode decreases and approaches the frequency of the first collective out-of-plane mode a coupling with this mode is activated.

Wind Energ. Sci. Discuss., doi:10.5194/wes-2016-53, 2016
Manuscript under review for journal Wind Energ. Sci.
Published: 23 December 2016

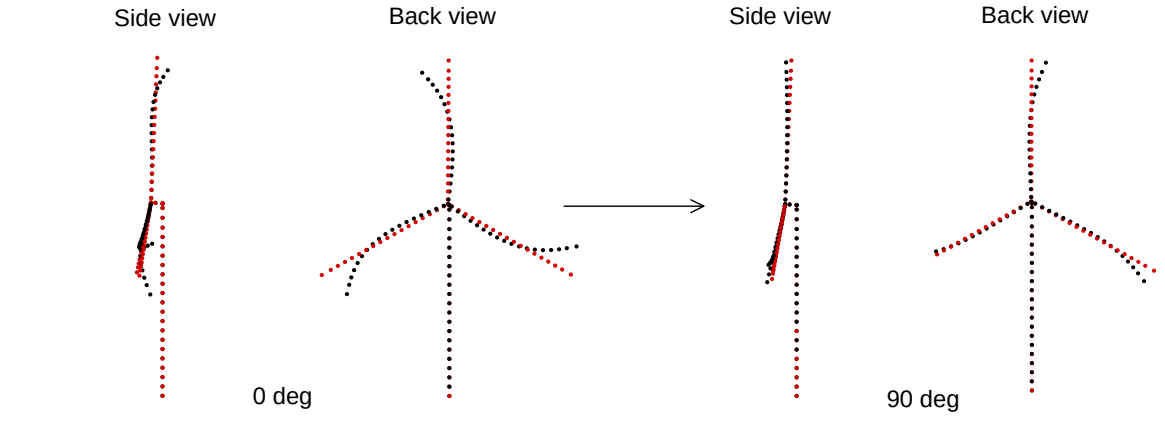

Figure 4. Mode shape alternation from 0^o to 90^o pitch for symmetric in-plane mode M8. Red symbols: undeformed state, Black symbols: deformed state.

As already discussed the AOAs experienced by the blades of an idling rotor vary significantly over the revolution. The velocity triangle of a section of an idling blade is illustrated in Figure 5 for the blade azimuth positions of 0^o, 90^o, 180^o and 270^o. It is seen that as a result of yaw error the AOA reaches a minimum/ maximum at $0^o/180^o$ azimuth respectively (whether the AOA will be positive or negative depends on the direction of the incoming flow – positive or negative yaw) while as a result of tilt and inflow inclination angles the AOA attains a minimum at 90^o and a maximum at 270^o. An example of the AOA variation of the 75% section of the reference 10 MW is shown in Figure 6 (a) for a yaw angle of 15^o and a tilt angle of 5^o. The mean wind speed and the pitch setting are taken equal to 42.5 ms^{-1} and 90^o respectively; the blade section is considered to have zero twist and the linear speed component due to the idling rotation of the blade is not taken into account (assuming an almost zero idling speed). It is seen that as the yaw angle increases the range of variation of the AOA equally increases. The range of variation of the AOA is equal to the yaw error angle. Moreover, superposition of inflow turbulence further increases the range of AOA variation. If the yaw error is combined with the tilt of the rotor (or the inclination of the mean inflow) then the range of variation of the AOA increases further. The azimuth angle for which maximum (positive or negative) AOA is obtained is shifted away from 0^o and 180^o given the 90^o phase difference of the two effects. Beyond a certain yaw angle the blade will definitely enter stall both in the positive and the negative AOAs regime.

As the pitch of the blade increases towards feather the local AOAs "seen" by the blade are equally shifted to lower values and therefore idling speed decreases. On the other hand reduction of the idling speed leads to higher AOAs along the blade span. An example of the effect of the idling speed on the AOAs of the 75% section is shown in Figure 6(b). For an inflow velocity of 42.5 ms^{-1} an almost 10^o increase of the AOAs is noted as the idling speed decreases from 1 RPM to almost 0 RPM. So, the pitch angle of the blade and the rotor idling speed are two interrelated but also competing parameters as concerns the mean level of the AOA variation.

Wind Energ. Sci. Discuss., doi:10.5194/wes-2016-53, 2016
Manuscript under review for journal Wind Energ. Sci.
Published: 23 December 2016

eawe european academy of wind energy
Open Access WIND ENERGY SCIENCE DISCUSSIONS

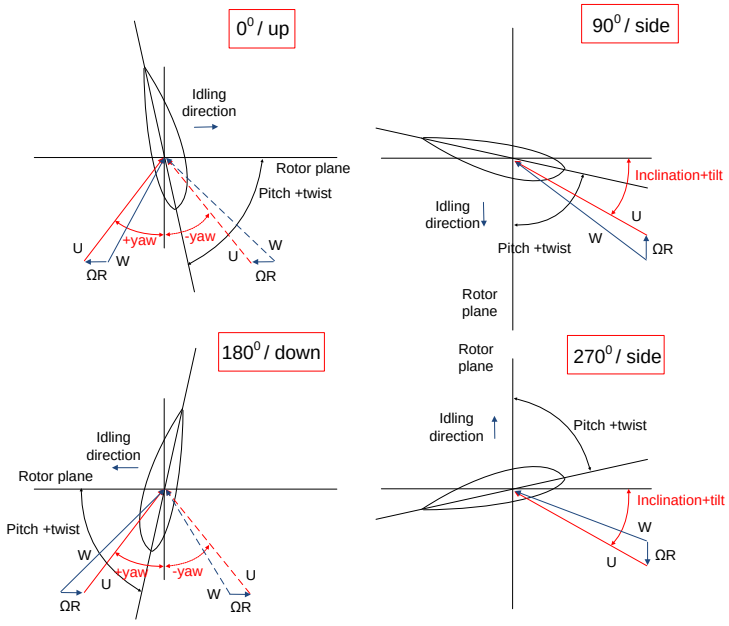

Figure 5. Velocity triangles of idling blade at different azimuth positions.

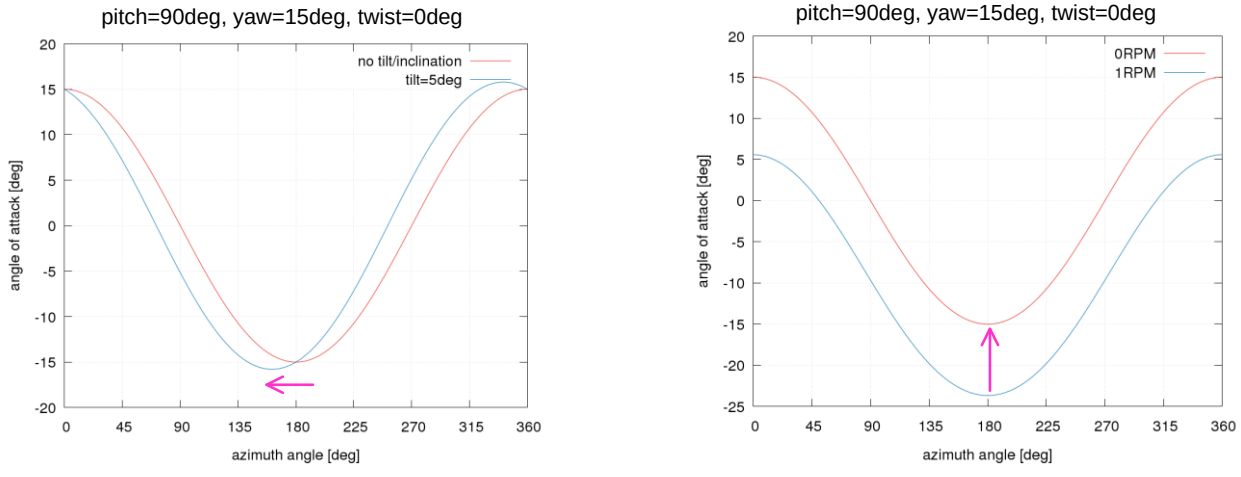

(a) **(b)**

Figure 6. Variation of the angle of attack over one revolution for a wind speed of 42.5 ms^{-1} (a) effect of yaw and tilt angle - tilt angle shifts the curve horizontally, the rotational speed is almost zero), (b) effect of rotational speed - the rotational speed shifts the curve vertically.

Whether stall induced vibrations will appear on an idling rotor, depends strongly on the post stall characteristics of the airfoil sections forming the blade. Higher negative slopes of the C_L curve and deeper drop of the C_L in the post stall region

Wind Energ. Sci. Discuss., doi:10.5194/wes-2016-53, 2016
Manuscript under review for journal Wind Energ. Sci.
Published: 23 December 2016

deteriorates stability characteristics. As already mentioned for moderate to high yaw angles the idling blade enters stall both at positive and negative AOAs. The post stall characteristics of cambered sections differ significantly between positive and negative AOA. Usually, airfoil sections exhibit smoother post stall behaviour at negative AOAs compared to that at positive ones (there are of course exceptions to the above statement). This implies that selection of the appropriate pitch setting and thereby of the appropriate idling speed could be critical in several cases when targeting the avoidance of stall induced vibrations. Adjustment of the blade pitch may shift the AOAs to a desired region.

3 Description of tools

Non-linear time domain aeroelastic simulations are performed using NTUA's in-house servo-aero-elastic solver hGAST (Manolas et al, 2015). Stability analysis is performed using the eigenvalue stability tool GAST_lin (Riziotis et al, 2004) which is a linearized version of the non-linear hGAST code. In both hGAST and GAST_lin solvers, the full wind turbine is considered as a multi-component dynamic system having as components the blades, the drive train and the tower; all approximated as Euler-Bernoulli or Timoshenko beam structures. Assembly of the above components into the full system is carried out in the framework of the so called multibody approach. It consists of considering each component separately from the others but subjected to specific free-body kinematic and loading conditions that are imposed at the connection points of the components.

In the multibody context, a local coordinate system $Oxyz$, (see Figure 7(a)) is assigned to each component/body with respect to which local elastic displacements are defined. In GAST_lin the local frame of each body is subjected to rigid body and elastic motions communicated by preceding bodies as kinematic conditions imposed at their connection points. Rigid body motions can be either prescribed or controlled while elastic motions consist of the total deflection of the previous components "transferred" to the current component. For example, the blades are subjected to pitch motion (rigid body motion directly imposed to the blade), azimuthal rotation and yaw rotation (rigid body motions indirectly imposed to the blades through the drive train and the nacelle) and the elastic translational and rotational motions of the drive train and the tower.

Let $\mathbf{r}_G^k$ denote the position of a point on the $k-th$ component with respect to the inertial (global) frame $O_G x_G y_G z_G$, $\mathbf{R}^k$ the position vector of the origin Oxyz of component "k" and $\mathbf{T}^k$ is the local to global rotation matrix (see Figure 7(a)). Then,

$$\mathbf{r}_G^k = \mathbf{R}^k + \mathbf{T}^k \cdot \mathbf{r}^k \tag{1}$$

$$\left(\mathbf{T}^k\right)^T \cdot \ddot{\mathbf{r}}_G^k = \underbrace{\left(\mathbf{T}^k\right)^T \cdot \ddot{\mathbf{R}}^k}_{\text{acceleration of the origin}} + \underbrace{\left(\mathbf{T}^k\right)^T \cdot \ddot{\mathbf{T}}^k \cdot \mathbf{r}}_{\text{centrifugal acceleration}} + \underbrace{2 \cdot \left(\mathbf{T}^k\right)^T \cdot \dot{\mathbf{A}}\mathbf{T}_k \cdot \dot{\mathbf{r}}_G}_{\text{Coriolis acceleration}} + \ddot{\mathbf{r}}^k \tag{2}$$

Wind Energ. Sci. Discuss., doi:10.5194/wes-2016-53, 2016
Manuscript under review for journal Wind Energ. Sci.
Published: 23 December 2016

eawe european academy of wind energy
Open Access WIND ENERGY SCIENCE DISCUSSIONS

where $\left(\mathbf{T}^k\right)^T \cdot \ddot{\mathbf{r}}_G^k$ is expressed in local coordinates. The motion of the local body system will give rise to extra inertial terms - centrifugal and Coriolis terms defined in Eq. (2) through the time derivatives of $\mathbf{T}^k$ - which must be added in the equilibrium equations.

In defining $\mathbf{R}^k$ and $\mathbf{T}^k$ a sequence of displacements and rotations $\mathbf{d}_j$ and $\mathbf{T}_j$ is followed that connects Oxyz to $O_G x_G y_G z_G$:

$$\mathbf{r}_G^k = \mathbf{d}_m + \mathbf{t}_m \cdot \left\{ ... \left[\mathbf{d}_2 + \mathbf{t}_2 \cdot \left(\mathbf{d}_1 + \mathbf{t}_1 \cdot \mathbf{r}^k \right) \right] \right\} \Rightarrow \mathbf{R}^k = \mathbf{d}_m + \mathbf{t}_m \cdot \left\{ ... \left[\mathbf{d}_2 + \mathbf{t}_2 \cdot \mathbf{d}_1 \right] \right\}, \quad \mathbf{T}^k = \prod_{j=1}^{J(k)} \mathbf{t}_j \tag{3}$$

Each of $\mathbf{d}_j$ and $\mathbf{t}_j$ is connected to either a single displacement or a single rotation in a certain direction. By collecting all displacements and rotations that are involved in the definition of $\mathbf{R}^k$ and $\mathbf{T}^k$, for all components, the vector of kinematic DOFs $\mathbf{q}$ is introduced. Each element of $\mathbf{q}$ is associated to a certain direction of rotation or translation and so $\mathbf{d}_j = \mathbf{d}_j(q_n; dir_n)$ corresponds to a q_n displacement in the dir_n direction and similarly for $\mathbf{t}_j$. The elements of $\mathbf{q}$ are in general time dependent and therefore $\mathbf{R}^k = \mathbf{R}^k(\mathbf{q_k}; t)$ and $\mathbf{T}^k = \mathbf{T}^k(\mathbf{q_k}; t)$ where $\mathbf{q}_k$ denotes the restriction of $\mathbf{q}$ for the $k-th$ component. If q_n refers to a controlled rigid body motion, then the corresponding dynamic equation is added to the system. If q_n is an already existing elastic DOF then a simple assignment equation is added. For example, the blades follow the elastic motion of the tower (Figure 7(b)) and so the tower top deflections are included in $\mathbf{q}$. Also the blades will follow the yawing of the nacelle, the rotation of the shaft and the pitch rotation, which are all included in $\mathbf{q}$ as DOFs of controlled motions. The motions of the supporting structures of a floating wind turbine and the teetering angle of two bladed rotors are also included as DOFs of free motions (see Figure 7(c)).

In addition to the kinematic conditions that are imposed at the connection points, loading conditions must be also satisfied. In particular, at each connection point, one of the connected bodies contributes the displacements and rotations to all others, which in turn contribute their internal (reaction) loads. So, in the previous example the tower will receive the loads from the nacelle.

The advantage of the above formulation in comparison to other multi-body formulations applying the Lagrange multipliers approach is that the resulting dynamic equations of motion can be easily linearized analytically and thereafter linear eigenvalue stability analysis can be performed with respect to a highly deflected steady or periodic state.

Wind Energ. Sci. Discuss., doi:10.5194/wes-2016-53, 2016
Manuscript under review for journal Wind Energ. Sci.
Published: 23 December 2016

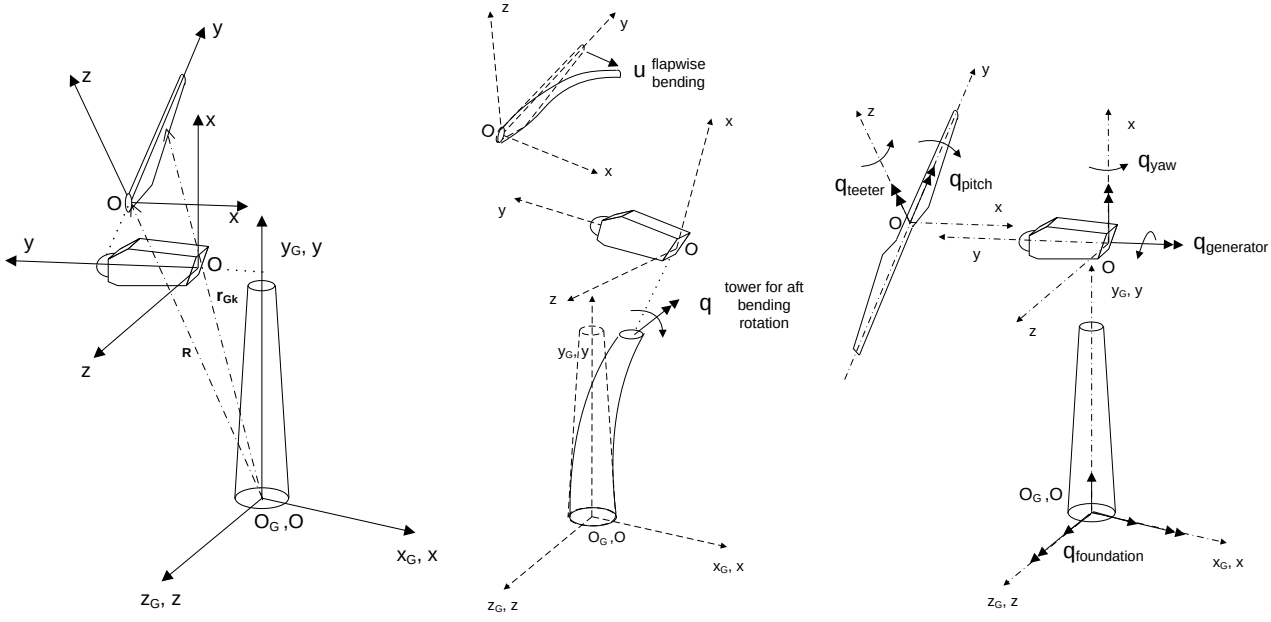

Figure 7. (a) Wind turbine inertial frame and local frame of the various components, (b) Realization of multibody kinematics, examples of elastic q DOFs ,(c) Realization of multibody kinematics, examples of controlled or free motion q DOFs.

The same multi-body formulation is also extendable to the component level which is actually implemented in hGAST. Highly flexible components, such as the blades, are divided into a number of interconnected sub-bodies, each considered as a single beam element or as an assembly of beam elements. Each sub-body has its own coordinate system $Oxyz$, which follows the deflection of the body. The first end (P1) of the sub-body is considered as the origin O while the second end (P2) is free. As illustrated in Figure 8, the co-ordinate system $Oxyz$ of the $\nu-th$ sub-body of the $k-th$ body, is defined with respect to the co-ordinate system $O_k x_k y_k z_k$ of the major body by the position vector of its origin $\tilde{\mathbf{R}}_\nu^k$ and a rotation matrix $\tilde{\mathbf{T}}_\nu^k$. Large deflections and rotations are gradually built and non-linear dynamics are introduced by imposing to each sub-body, the deflections and rotations of preceding sub-bodies as rigid body motions. In particular, a vector $\tilde{\mathbf{q}}_\nu^k$ is defined for each $\nu-th$ sub-body of the $k-th$ body that contains the deflections (translations and rotations of the free ends) of the preceding sub-bodies: $\tilde{\mathbf{R}}_\nu^k = \tilde{\mathbf{R}}_\nu^k(\tilde{\mathbf{q}}_\nu^k; t)$ and $\tilde{\mathbf{T}}_\nu^k = \tilde{\mathbf{T}}_\nu^k(\tilde{\mathbf{q}}_\nu^k; t)$.

If the main body is divided into a sufficiently large number of sub-bodies, then deflections and rotations, with respect to the sub-body system, are considered small and linear beam equations can be employed. The position vector of the arbitrary point on the $\nu-th$ sub-body of the $k-th$ body is written with respect to the inertial frame $O_G x_G y_G z_G$ as:

Wind Energ. Sci. Discuss., doi:10.5194/wes-2016-53, 2016
Manuscript under review for journal Wind Energ. Sci.
Published: 23 December 2016

$$\mathbf{r}_{G,v}^{k} = \mathbf{R}^{k}(\mathbf{q}_{k};t) + \mathbf{T}^{k}(\mathbf{q}_{k};t)\cdot\left\{\tilde{\mathbf{R}}_{v}^{k}(\tilde{\mathbf{q}}_{v}^{k};t) + \tilde{\mathbf{T}}_{v}^{k}(\tilde{\mathbf{q}}_{v}^{k};t)\cdot\mathbf{r}_{v}^{k}\right\} \quad (4)$$

where $\mathbf{r}_{v}^{k}$ is the position vector of the arbitrary location on the sub-body with respect to $Oxyz$. Dynamic coupling of the sub-bodies is introduced by communicating the reaction loads (3 forces and 3 moments) at the first node of each sub-body to the free node of the previous sub-body as external load (see Figure 8).

Rotor aerodynamics in both codes is simulated using a Blade Element Momentum (BEM) model. In hGAST an elaborated BEM model is employed that accounts for dynamic inflow, yaw misalignment, and dynamic stall effect through the ONERA dynamic stall model (Petot, 1989). In GAST_lin the frozen wake concept is adopted while unsteady aerodynamics and dynamic stall effect are again accounted for by means of the ONERA model. In the linearized tool, the unsteady aerodynamic and dynamic stall equations, the corresponding aerodynamic states (circulation parameters of the ONERA model) and the structural equations along with the corresponding DOFs are treated uniformly in one system following the so-called "Aeroelastic Beam Element" concept (Riziotis et al, 2004).

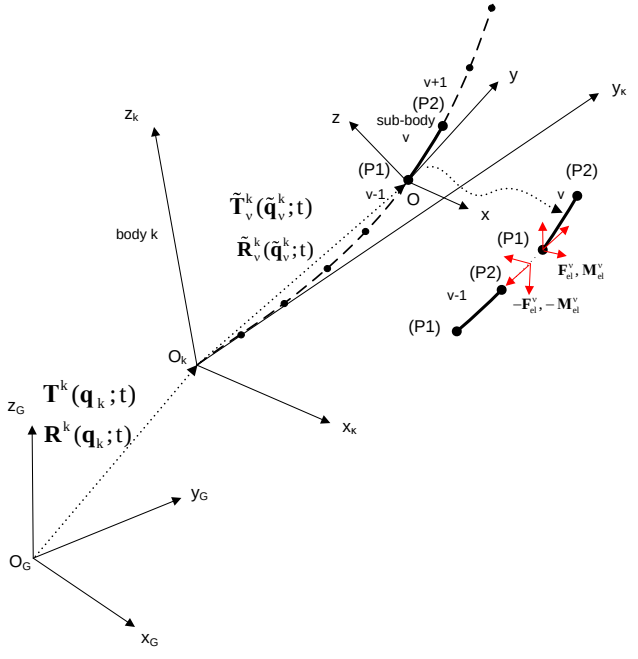

Figure 8. Realization of multibody kinematics at the level of the component.

In normal operating conditions stability analysis is performed in the context of multi-blade transformation (Coleman & Feingold, 1958). As already discussed in the introduction section stability analysis of a rotating rotor experiencing yawed inflow would require application of Floquet's theory. This is because periodic coefficients arising from the asymmetry of aerodynamic loads cannot be eliminated by means of Coleman's transformation. However, given that idling speeds are usually small (~1 RPM) and in order to avoid computationally expensive Floquet analysis, stability simulations are

Wind Energ. Sci. Discuss., doi:10.5194/wes-2016-53, 2016
Manuscript under review for journal Wind Energ. Sci.
Published: 23 December 2016

performed for a static rotor at different azimuth angles. Azimuth positions in the range [0°, 120°] are considered that correspond to one third of the rotor revolution. Although the rotor is considered static, a free rotation boundary condition is imposed at the generator side in order to approximate as closely as possible idling operation. Also the average idling rotational speed which has been obtained through the time domain analyses, is taken into account in forming the local to the blade sections velocity triangles and in calculating the induction parameters.

4 Results and discussion

4.1 Time-domain analysis results

Time domain aeroelastic simulations in turbulent inflow are performed for the Reference 10 MW wind turbine, at a mean wind speed of 42.5 ms^{-1}, with a turbulence intensity (TI) 11%, for various yaw misalignment angles in the range [-60°, +60°] and constant pitch angle of 87°. Six 10-minute simulations are performed for every yaw angle corresponding to different realizations of the wind (wind seeds). Figure 9 presents the min-max envelope of the edgewise (out-of-plane) bending moments at blade root as functions of the yaw misalignment angle. Load results of all three blades for the different wind seeds, as well as average loads are provided in the plot. It is seen that ultimate loads attain both maximum and minimum value at +30º of yaw. When loads are averaged, the minimum is found at +22.5° of yaw (very close though to the load at +30° of yaw) while the maximum is still obtained at +30° yaw angle.

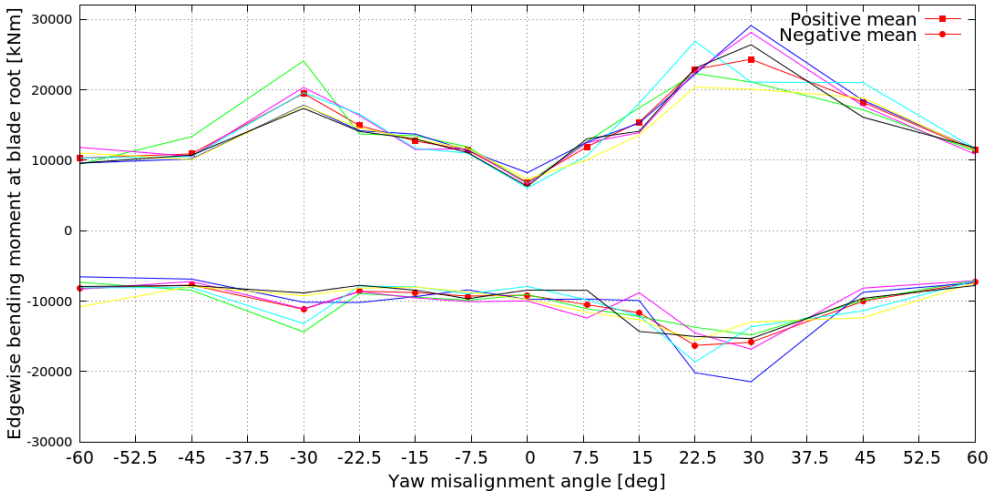

Figure 9. Ultimate blade root edgewise bending moments. Loads from 6 wind seeds are averaged. Wind speed 42.5 ms^{-1}; TI=11%; yaw angles in the range [-60°, +60°].

For the yaw angle of 30° a pattern of the edgewise bending moments at the three blade roots is shown in Figure 10 along with the time series of the azimuth angle and the AOA for a 45s duration. The average idling speed of the rotor is about 0.8 RPM at the above conditions (wind speed 42.5 ms^{-1} and yaw 30°). Also in Figure 11, the obtained C_L values at r/R=90%

Wind Energ. Sci. Discuss., doi:10.5194/wes-2016-53, 2016
Manuscript under review for journal Wind Energ. Sci.
Published: 23 December 2016

are collected and plotted with respect to the corresponding AOA. In this plot, the regions of unfavourable lift slope are marked in grey.

At t=107s (marked with a dashed blue line in Figure 10), mild edgewise vibrations start to grow on blade 3 as a result of increasing AOA that push the blade into stall. At t=107s rotor azimuth is 90^o (rotor azimuth is defined as the azimuth angle of the blade that lies in the sector [0^o, 120^o] – blade 1 in this case). It is noted that 0^o azimuth corresponds to a blade being at 12 o'clock. The AOA on blade 3 crosses the level of 15^o so stall takes place at positive AOA. Blade 2 also operates in deep stall experiencing negative AOA in the range [-30^o, -40^o]. Finally, the flow remains attached on blade 1. The AOAs experienced by blade 1 remain at about -10^o AOA for approximately 5 s and so no vibrations are expected for this blade within this time interval.

Progressing in time, the situation is changing. At t=116 s (marked by a red dashed line), mild edgewise vibrations now start to grow on blade 1 as a result of increasing AOA that push this blade into stall at the negative AOAs regime. As indicated in Figure 10, at t=116 s, the azimuth angle of the rotor is 20^o and the AOA "seen" by blade 1 grows to about -30^o. As time evolves (time period [116s,120s]), blade 1 goes deeper into negative AOA stall (about -40^o) while over the same time period, blade 3 stays within deep stall experiencing AOA in the range [20^o,30^o]. This explains why blade 3 exhibits large vibrations over the whole time period [107 s, 120 s]. Recovery to attached flow conditions is only obtained for blade 3 at t>120 s. Opposite to the other two blades, now blade 2 operates in attached flow conditions (AOA~ -15^o).

Looking back in time, at the time interval [80 s, 95 s], it can be seen that blade 1 is experiencing similar flow conditions to those experienced by blade 3 in the time interval [107 s, 115 s]. Blade 2 is now lying in the azimuth range of 80^o-100^o. The only difference with respect to the time period [107 s, 115 s] is that now the rotor speed is lower and therefore blade 1 remains longer within the stall region. High load amplitudes are obtained for blade 1 within this time interval that decrease when blade 1 moves away from stall (AOA and loads of blade 1 decrease in the time interval [95 s, 105 s]).

4.2 Eigenvalue analysis results

In the present section eigenvalue stability analysis results for the idling rotor are presented at the wind velocity of 42.5 ms^{-1} and for various yaw angles in the range [0^o, 60^o]. The average idling speed versus yaw angle in the stability simulations was taken from the time domain analysis results by averaging the mean rotor speed of the six realizations performed for every yaw angle. The results of the mean idling speed as function of the yaw angle are shown in Figure 12. Emphasis is put on yaw angles for which higher minimum/maximum loads are predicted by non–linear time domain analysis. A correlation is attempted between the damping and frequency predictions obtained through the eigenvalue stability simulations with the results of the time domain analysis. Eigenvalue stability simulations are performed using both steady-state and unsteady (ONERA model) aerodynamics. Certain engineering dynamic stall models (e.g. Beddoes-Leishman) automatically switch to almost steady-state aerodynamics at very high AOA (well beyond CLmax AOA) (see Hansen et al, 2004) while ONERA model is fully deployed at all AOA. Therefore, an analysis using steady state polars is meaningful because it provides the range of anticipated damping predictions among different models.

Wind Energ. Sci. Discuss., doi:10.5194/wes-2016-53, 2016
Manuscript under review for journal Wind Energ. Sci.
Published: 23 December 2016

eawe european academy of wind energy
Open Access WIND ENERGY SCIENCE DISCUSSIONS

The modal frequencies and damping (in logarithmic decrement) of the rotor modes (M3-M8) at 0^o yaw are shown in Figure 13(a)&(b) as functions of the rotor azimuth angle in the range of [0^o, 120^o] (azimuth angle of blade 1). Results are obtained using unsteady aerodynamics model. In Figure 14(a)&(b) the PSDs of the flapwise and edgewise bending moments coming from the earlier presented time domain simulations are also provided for the same yaw angle.

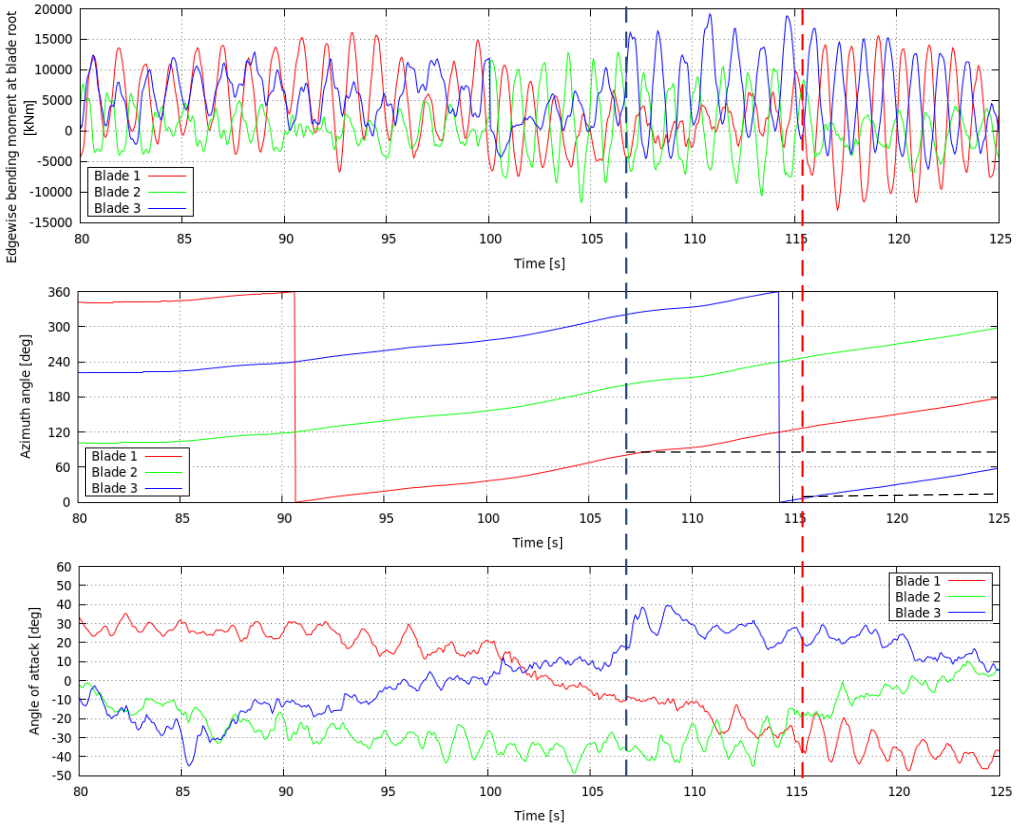

Figure 10. Times series of blade root edgewise bending moment, blade azimuth angle and angle of attack at r/R=0.90 spanwise position. Wind speed 42.5 ms^{-1}, TI 11%, yaw angle 30^o.

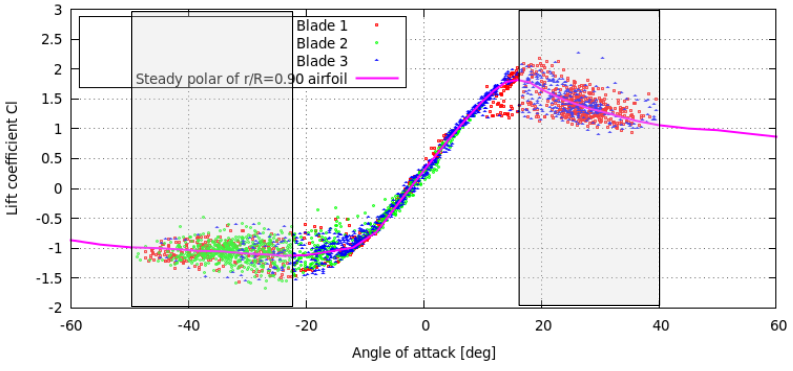

Figure 11. CL - AOA plot at r/R=0.90 spanwise position. Wind speed 42.5 ms^{-1}, TI 11%, yaw angle 30^o.

Wind Energ. Sci. Discuss., doi:10.5194/wes-2016-53, 2016
Manuscript under review for journal Wind Energ. Sci.
Published: 23 December 2016

It is seen that the three out-of-plane modes, M5, M6 and M7, are clearly the lowest damped ones (Figure 13(b)). This is definitely in agreement with the time domain analysis results as shown in the PSD plots of the edgewise bending moment at the root of the three blades (Figure 14(b)). The three predominant peaks on the PSD plot indicate the modes that are highly excited. The corresponding frequencies are found at ~0.69 Hz, 0.81 Hz, 0.95 Hz. These frequencies agree well with the values obtained with the stability tool (Figure 13(a)). A lower peak appears at 0.25 Hz which corresponds to the first longitudinal tower bending mode M1. On the contrary no peak appears in the PSD of the blade root flapwise bending moment (Figure 14(a)). This indicates that the aerodynamic damping of the in-plane modes M3, M4 and M8 is high. The same is also consistently predicted by the stability tool (all values are above 100% in logarithmic decrement). Worth noticing is that both the level of damping and the frequencies are independent of the azimuth position in the 0^o yaw case. Eigenvalue analysis using steady-state polars (not shown in the figures) gives similar results with those of the unsteady aerodynamic analysis. The damping of the low damped out-of-plane (edgewise) modes M5, M6 and M7 remains positive at all azimuth angles while in-plane (flapwise) modes appear to have about 50% higher damping and 20% lower frequency. The damping and frequencies are almost independent of the azimuth angle also when steady-state aerodynamics is used.

Figure 15(a)&(b) present frequency and damping results for the yaw angle of 30^o using steady-state aerodynamics. The same set of results using unsteady aerodynamics is presented in Figure 16(a)&(b). Figure 17(a)&(b) give the PSDs of the flapwise and edgewise bending moments at the blade root of the three blades as predicted through non-linear time domain analysis. It is reminded that according to the time domain analysis results of Sect. 4.1, at 30^o yaw the edgewise loads reach their maximum values. Also as explained in Sect. 2, for this high yaw angle the AOAs experienced by the rotating blades will significantly vary with the azimuth angle. As a result the modal frequencies and damping also vary over the revolution in contrast to the 0^o yaw case. At very high yaw angles, the AOAs seen by the blades are expected to enter post stall on both sides of the polar (positive and negative AOAs).

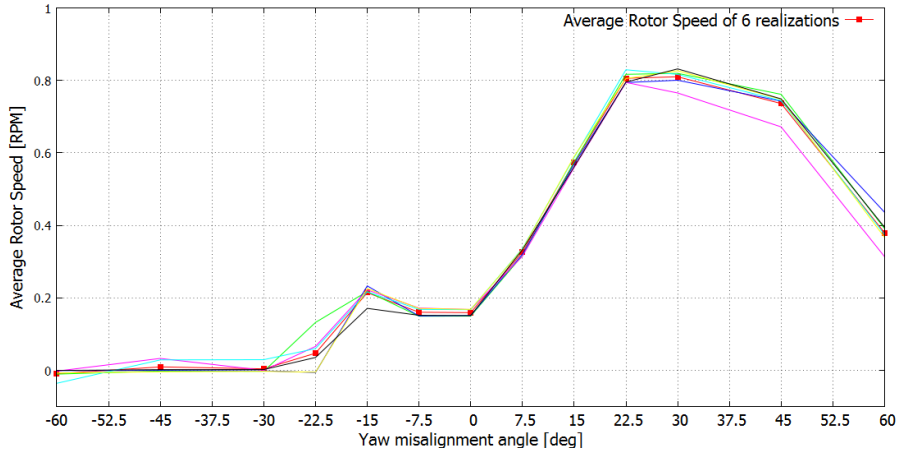

Figure 12. Rotor idling speed vs. yaw angle for the pitch angle of 87^o

Wind Energ. Sci. Discuss., doi:10.5194/wes-2016-53, 2016
Manuscript under review for journal Wind Energ. Sci.
Published: 23 December 2016

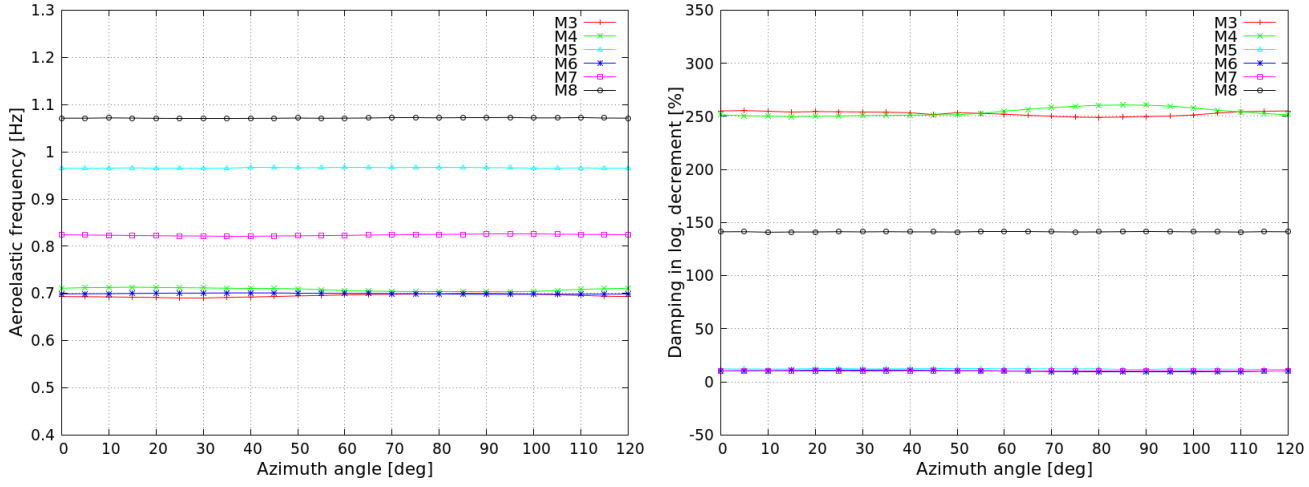

(a) **(b)**

Figure 13. (a) Modal frequency & (b) modal damping of rotor modes vs. azimuth angle, at U=42.5 ms^{-1} and yaw=0° (Unsteady aerodynamics through ONERA model).

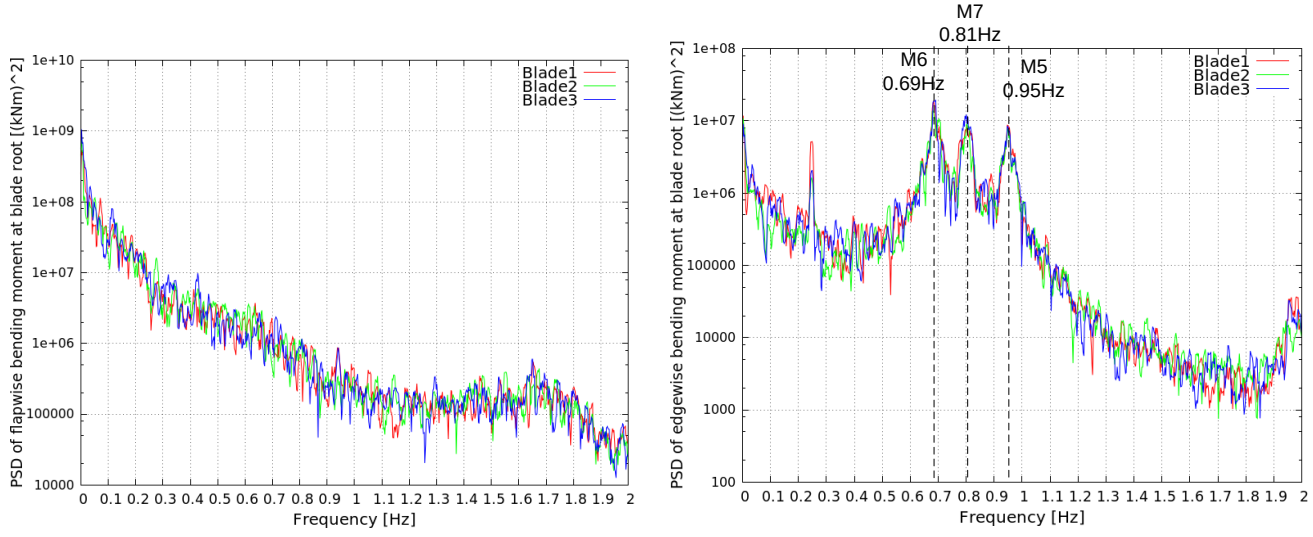

(a) **(b)**

Figure 14. (a) PSD of the flapwise bending moment at the blade root & (b) PSD of the edgewise bending moment at the blade root, at U=42.5 ms^{-1} and yaw=0°.

Wind Energ. Sci. Discuss., doi:10.5194/wes-2016-53, 2016
Manuscript under review for journal Wind Energ. Sci.
Published: 23 December 2016

As compared to the 0^o yaw case, lower damping values are obtained for most modes (in-plane and out-of-plane). This indicates that stall induced vibrations start to develop at the yaw angle of 30^o. The damping of the in-plane modes M3, M4 and M8 significantly drops. The damping of M4 (asymmetric flap tilt/horizontal mode) becomes even negative at certain azimuth angles. When steady-state polars are used, the damping of M4 is negative at the azimuth ranges $[0^o,25^o]$ and $[75^o,120^o]$. Almost constant, high negative damping values of about -25% are obtained for M4 in the above azimuth ranges. When ONERA unsteady aerodynamic model is used the damping becomes locally negative only at the azimuth angles of 0^o and 100^o. Despite the negative damping values of M4, damping remains highly positive (up to 150%) over a wide azimuth range of $[30^o,70^o]$. This suggests that the overall damping of the in-plane modes will be eventually positive. On the other hand, modes M5, M6, M7 still have low or negative damping throughout the entire range of azimuth angles. Especially for M7 (asymmetric edge horizontal/tilt mode) the damping is negative at all azimuth angles both for steady-state and unsteady aerodynamics. Comparing the two aerodynamic models, the damping of M7 is lower at all azimuth angles when steady state-polars are used. For M5 and M6 the damping predicted with unsteady aerodynamics remains low but positive at all azimuth angles while with steady-state aerodynamics the damping is negative in the azimuth ranges $[0^o,20^o]$ and $[90^o,120^o]$.

The stability results that used unsteady aerodynamic modelling are in line with the observations made in the time domain analysis of the previous section. In agreement with the time domain analysis results higher negative damping values are noted over the azimuth ranges $[0^o, 20^o]$ and $[75^o, 110^o]$ (azimuth ranges where higher vibrations have been observed in time domain results). Again four peaks dominate the PSD plot of the edgewise bending moment at 0.25 Hz, 0.7 Hz, 0.8 Hz and 0.95 Hz (see Figure 17(b)). The first one corresponds to the first tower longitudinal bending mode M1 while the other three correspond to the three edgewise (out-of-plane) modes M5, M6, M7. Again, the frequencies of the highly excited modes in the results of the time domain analysis agree well with the frequencies predicted by the stability tool (Figure 16(a)) for the low damped rotor out-of-plane modes. The largest peak is seen at the frequency of 0.8 Hz (the frequency of M7) indicating that indeed this is the lowest damped mode of the rotor. A closer look in the vicinity of the 0.8 Hz peak (see focus plot Figure 18(a)) reveals two additional peaks around the centre frequency of 0.8 Hz with a frequency shift of about $\pm 0.01\,\mathrm{Hz}$. The above frequency shift corresponds to the average idling rotational frequency (1p frequency). These peaks represent rotating periodic dynamics of the system (in terms of the principle eigenfrequency) and they are found to be even more excited than the centre frequency peak. Such peaks are not observed in the PSD plot of the 0^o yaw case since the idling speed of the rotor is almost zero in this case, as seen in Figure 12. In a simulation with uniform inflow, at the same wind speed ($42.5\ \mathrm{ms}^{-1}$), the abovementioned peaks become more distinct (other peaks appear as well that correspond to higher multiples) as seen in the PSD plot of Figure 18(b). It is noted that in the uniform inflow case, after an initial transient, the idling speed reaches a constant value (0.78 RPM, 0.013 Hz) This explains why the two peaks appear at frequencies exactly equal to $\pm\omega$ of the principle eigenvalue. In the case of turbulent wind, the idling speed continuously changes and therefore the obtained peaks are more spread. The amplifying response of the edgewise moment in the simulation with uniform inflow shown in Figure 19 indicates that under uniform inflow conditions the system is unstable. The above result is in perfect agreement with the results of the eigenvalue analysis which show that M7 mode is negatively damped at all azimuth angles. In turbulent

Wind Energ. Sci. Discuss., doi:10.5194/wes-2016-53, 2016
Manuscript under review for journal Wind Energ. Sci.
Published: 23 December 2016

wind simulations instabilities are mitigated as a result of the incoherent loading of the blades along their span and the continuous variation of the inflow that pushes the blade in and out stall (regions of negative C_L slope).

In Figure 17(a) high energy levels are noted in the frequency range of [0.5 Hz, 0.6 Hz]. The peak corresponds to the in-plane mode M4. As discussed earlier, according to the stability predictions, this is the lowest damped flapwise mode. The smooth shape and the spread of the peak indicate the high aerodynamic damping involved.

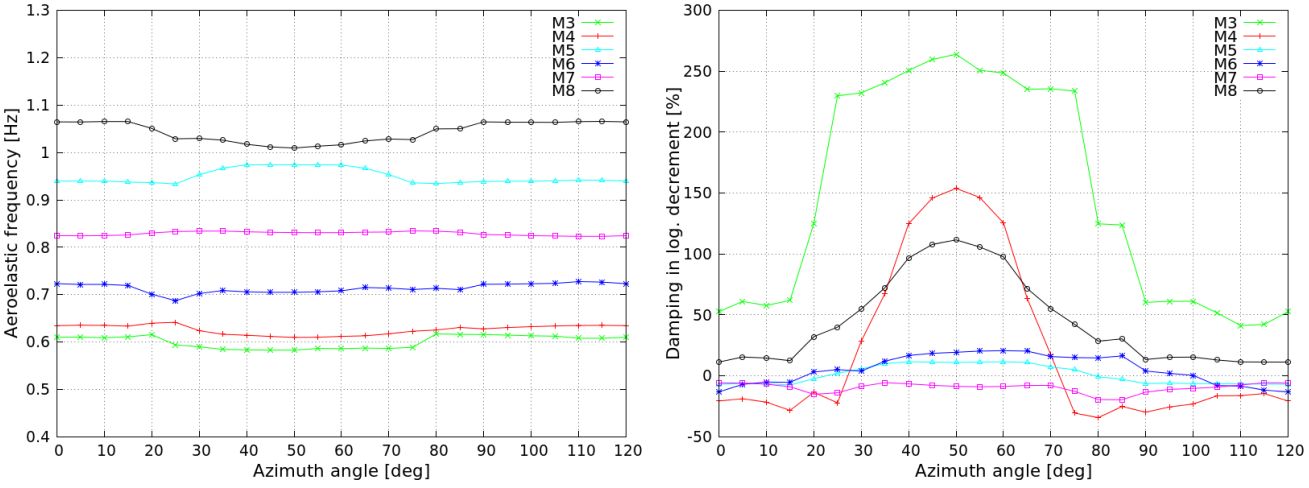

Figure 15. (a) Modal frequency & (b) modal damping of rotor modes vs. azimuth angle, at U=42.5 ms^{-1} and yaw=30° (Steady-state aerodynamics).

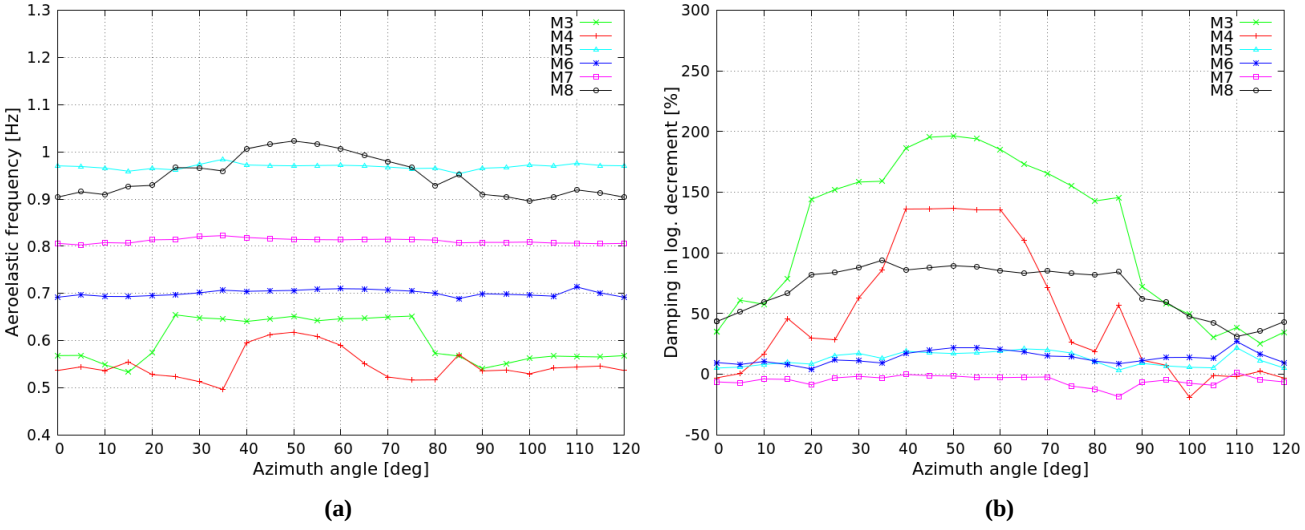

Figure 16. (a) Modal frequency & (b) modal damping of rotor modes vs. azimuth angle, at U=42.5 ms^{-1} and yaw=30° (Unsteady aerodynamics through ONERA model).

Wind Energ. Sci. Discuss., doi:10.5194/wes-2016-53, 2016
Manuscript under review for journal Wind Energ. Sci.
Published: 23 December 2016

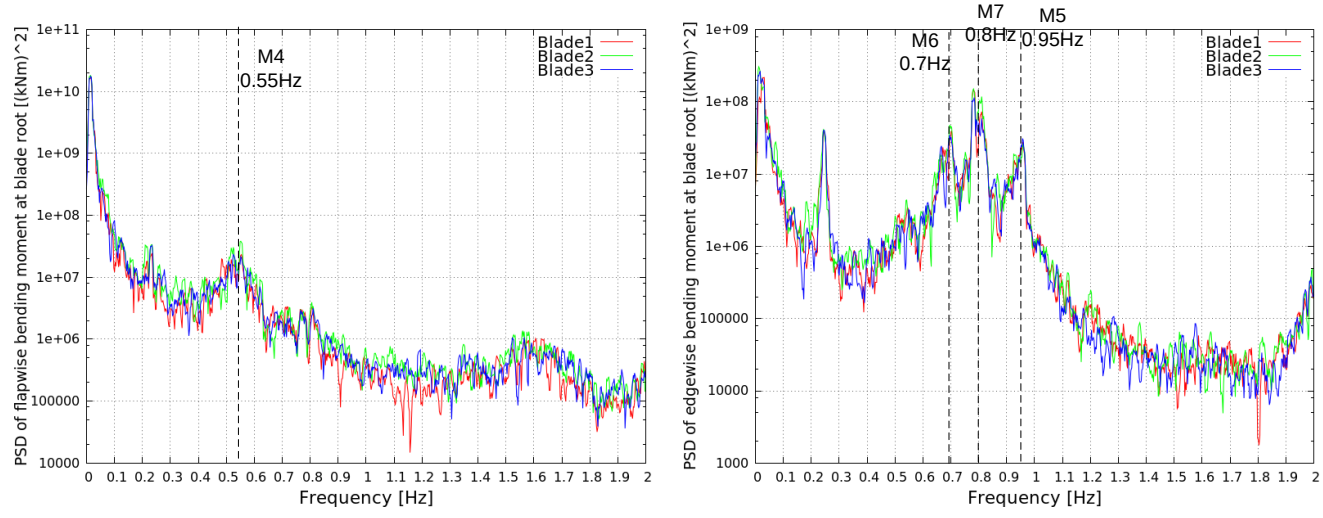

(a) **(b)**

Figure 17. (a) PSD of the flapwise bending moment at the blade root & (b) PSD of the edgewise bending moment at the blade root, at U=42.5 ms^{-1} and yaw=30°.

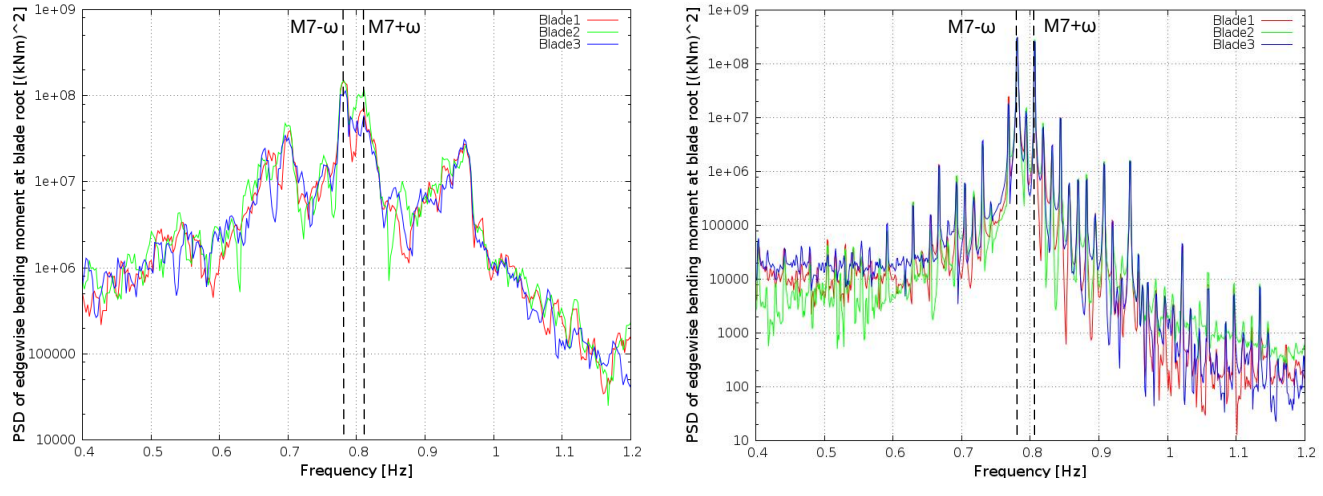

(a) **(b)**

Figure 18. PSD of the edgewise bending moment at the blade root, at U=42.5 ms^{-1} and yaw=30° (a) Turbulent inflow (focus plot) & (b) Uniform inflow (focus plot).

Wind Energ. Sci. Discuss., doi:10.5194/wes-2016-53, 2016
Manuscript under review for journal Wind Energ. Sci.
Published: 23 December 2016

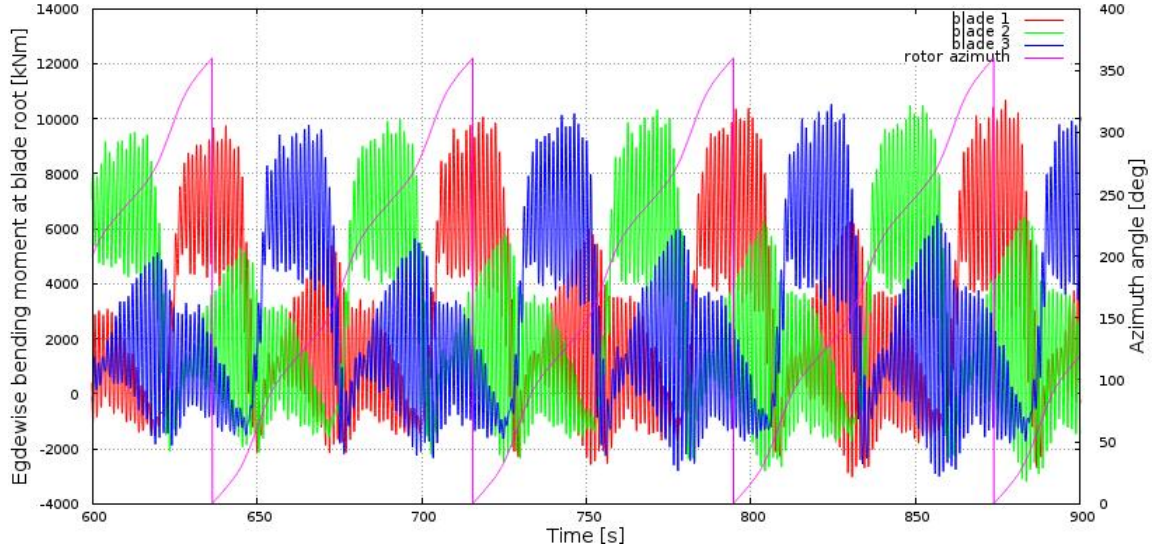

Figure 19. Time series of the edgewise bending moment at the blade root, with uniform inflow at U=42.5 ms^{-1} and yaw=30°.

In Figure 20 and Figure 21 the damping results for the 45° and 60° yaw cases are shown. Results for both steady and unsteady aerodynamics are compared. For yaw angles higher than 30° the system stability is gradually restored. This is in agreement with the results of the time domain analysis which showed a gradual decrease of the edgewise loads beyond the 30° yaw angle. At the yaw angle of 45° (see Figure 20) the damping of M7 increases as compared to the 30° yaw case. The damping as predicted with steady-state aerodynamics is negative but very close to zero for all azimuth angles while unsteady aerodynamic analysis always gives positive damping. The lowest damped mode, both with steady and unsteady aerodynamics, appears now to be M6 (asymmetric edge vertical/yaw mode). Negative values are obtained in the azimuth range [105°,120°] (also in the range [0°,10°] with steady-state aerodynamics). The damping of M4 appears to have a negative dip at 55° azimuth angle in the steady-state results which is smeared out in unsteady computations. Overall the damping of the in-plane modes seems to decrease as the yaw angle increases however still remains highly positive over a wide range of azimuth angles.

Damping results at the yaw angle of 60° using steady-state aerodynamics (see Figure 21(a)) are found to be very similar to those of the 45° yaw case. Unsteady results (see Figure 21(b)) indicate that the damping of M7 continues to increase as the yaw angle increases. The same holds with mode M6. It is noted that all out-of-plane modes are positively damped at 60° of yaw while M6 is the mode with the lowest damping characteristics.

Wind Energ. Sci. Discuss., doi:10.5194/wes-2016-53, 2016
Manuscript under review for journal Wind Energ. Sci.
Published: 23 December 2016

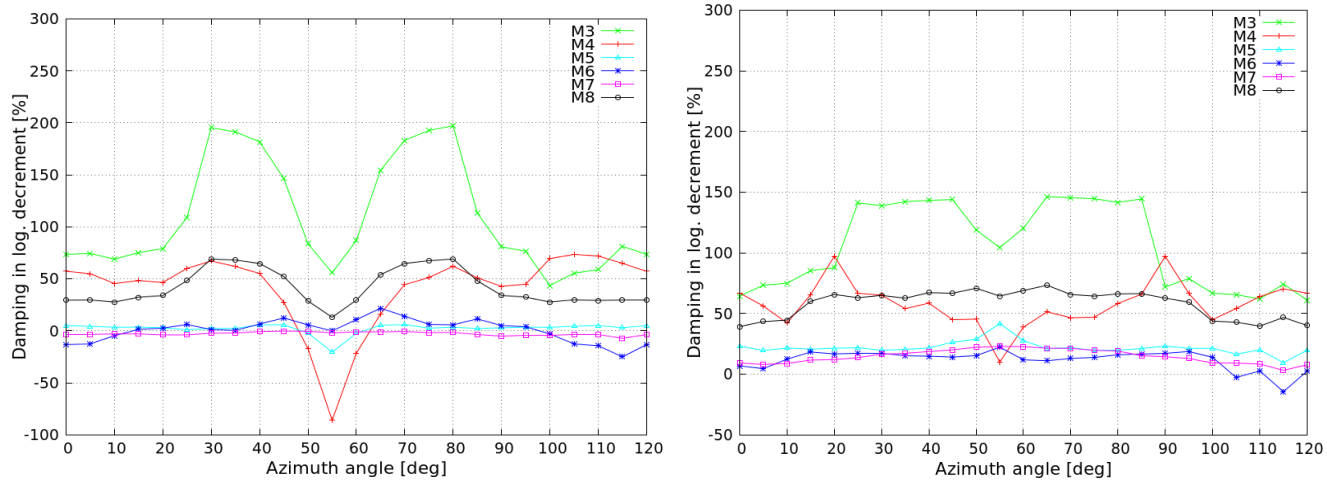

(a) **(b)**

Figure 20. Modal damping of rotor modes vs. azimuth angle at U=42.5 ms^{-1} and yaw=45^{o} (a) Steady-state aerodynamics (b) unsteady aerodynamics (ONERA).

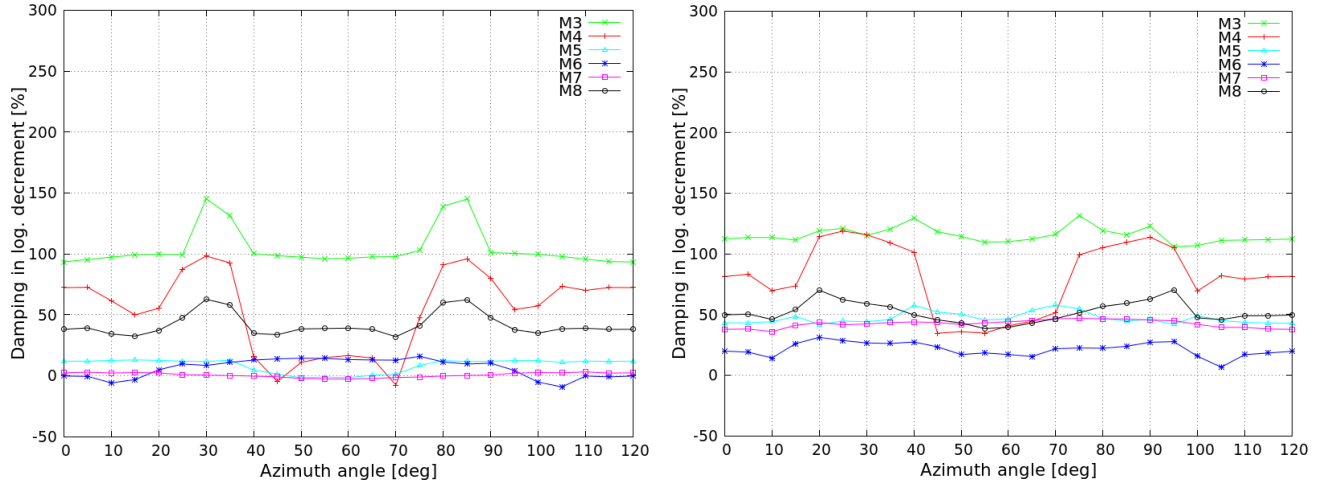

(a) **(b)**

Figure 21. Modal damping of rotor modes vs. azimuth angle at U=42.5 ms^{-1} and yaw=60^{o} (a) Steady-state aerodynamics (b) unsteady aerodynamics (ONERA).

4.3 Work computation results

Next, the results of the eigenvalue analysis of the previous section are further evaluated by computations of the work of the aerodynamic forces in imposed harmonic vibrations. The blade is subjected to an externally imposed harmonic motion following the shape and frequency of the mode considered and the unsteady aerodynamic loads are calculated along its span

Wind Energ. Sci. Discuss., doi:10.5194/wes-2016-53, 2016
Manuscript under review for journal Wind Energ. Sci.
Published: 23 December 2016

at various stations. Then the work done by the aerodynamic loads is computed over one cycle of the blade oscillation. The above work is directly associated with the damping of the corresponding mode. The mode shapes and eigen-frequencies used in the present analysis are the aeroelastic ones obtained through the eigenvalue analysis on the full aeroelastic system. As opposed to the structural mode shapes (obtained for the free vibration problem in vacuum conditions), the aeroelastic mode shapes also include the phase shift between the various components of the blade motion and therefore provide more realistic prediction of the work distribution.

Work analysis is able to bring more insight into stability computations because it provides stability characteristics separately for each blade. When eigenvalue analysis gives negative damping value for a specific mode, work analysis can identify which blade is responsible for the instability as well as the spanwise extent of the negative damping contribution. The non-linear behaviour of the aerodynamic loads can be also investigated, by changing the amplitude of the forced oscillation. Since one of the main objectives of the present work is the evaluation of the linear eigenvalue analysis predictions, modal amplitude was kept low and equal to 0.2 m at the blade tip. As previously the analysis focuses on the yaw angle of 30^o where stall induced vibrations mainly take place and only on rotor modes.

In Figure 22 & Figure 23 aerodynamic work results (integrated over the span and summed up for the three blades) are compared against eigenvalue analysis results both for steady-state and unsteady aerodynamics. The cross comparison of the two sets can be only performed at a qualitative level because in order to obtain the non-linear damping of a particular mode through work computations the predicted work value must be divided by the modal mass of the mode which is not the same for the different modes.

For steady-state aerodynamics (see Figure 22) the agreement between work computations and eigenvalue analysis results is very good. Some differences are only noted in the shape of the work distribution of M4. Eigenvalue analysis predicts almost constant high positive damping of about 250% in the azimuth range [25^o, 75^o]. In work results although high work values are obtained in the same azimuth range a peak value is predicted at the azimuth angle of 50^o. As in the eigenvalue analysis M8 remains positively damped at all azimuth angles while M3 exhibits negative damping values in the azimuth ranges [0^o, 25^o] and [75^o, 120^o]. Both methods agree that the damping of M7 is negative at all azimuth angles and that M5 and M6 are mostly positively damped. For unsteady aerodynamics (see Figure 23) and in regard to the flap modes, in general the two sets correlate well except for M3 at some specific azimuths (for example 5^o and 115^o). In these particular positions the eigenvalue analysis predicts positive damping, while in the work analysis the damping is negative. Also, in regard to the edgewise modes, the two methods compare well. In line with the eigenvalue analysis results, the work calculated for mode M7 remains negative over the whole azimuth range whereas the same calculation for M5 and M6 gives positive work values. It is noted that differences between eigenvalue analysis and work results in the shape of the curves are bigger in the case of unsteady aerodynamics. Despite the relatively small amplitude of 0.2 m used in the work analysis deviations from the eigenvalue analysis results are big in some cases. The explanation of the above differences lies in the strong non-linearity of the ONERA equations, especially within the stall region. In ONERA model, dynamic stall characteristics are derived through the solution of a set of second order in time, variable coefficient (coefficients depend on steady-state polars)

Wind Energ. Sci. Discuss., doi:10.5194/wes-2016-53, 2016
Manuscript under review for journal Wind Energ. Sci.
Published: 23 December 2016

differential equations. In regions where the gradient of the steady-state polars changes rapidly the linearized set of equations fails to represent correctly the actual non-linear set.

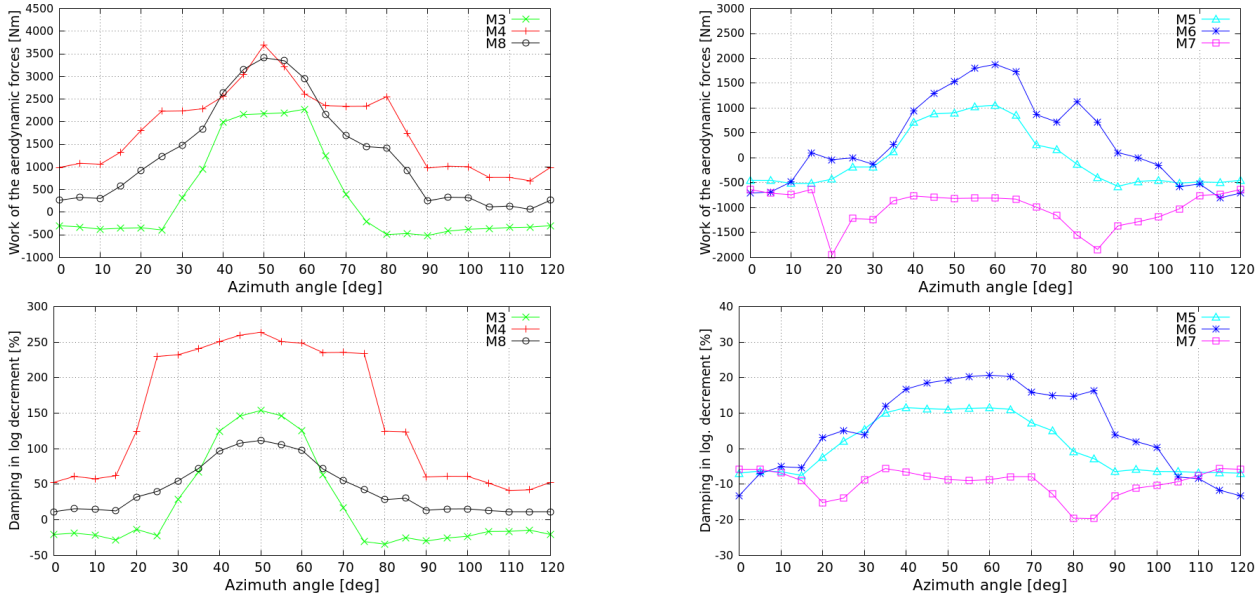

(a) **(b)**

Figure 22. Comparison between aerodynamic work (0.2m modal amplitude) and damping results versus azimuth angle for steady-state aerodynamics; U=42.5 ms^{-1} and yaw=30^{o}. (a) in-plane (flapwise) modes, (b) out-of-plane (edgewise modes)

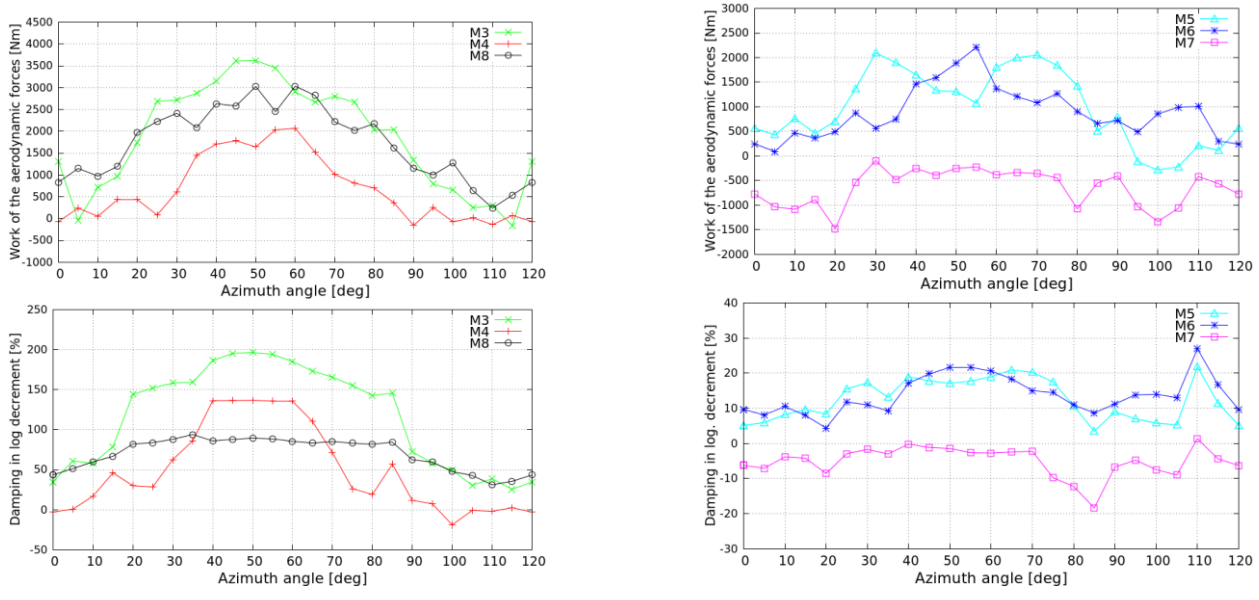

(a) **(b)**

Figure 23. Comparison between aerodynamic work (0.2m modal amplitude) and damping results versus azimuth angle for unsteady aerodynamics (ONERA model); U=42.5 ms^{-1} and yaw=30^{o}. (a) in-plane (flapwise) modes, (b) out-of-plane (edgewise modes)

Wind Energ. Sci. Discuss., doi:10.5194/wes-2016-53, 2016
Manuscript under review for journal Wind Energ. Sci.
Published: 23 December 2016

eawe european academy of wind energy
Open Access WIND ENERGY SCIENCE DISCUSSIONS

In Figure 24 a snapshot of the shape of the negatively damped M7 mode is shown along with the traces of the three blades tip motion. Clearly, the mode is an asymmetric, out-of-plane one with the two lower blades moving in one direction while the upper in the opposite. Modal motion resembles tilting of the rotor and that is why the mode is called asymmetric out-of-plane tilt. It is seen that the three blades undergo a coupled edgewise/flapwise motion (elliptical shape of modal displacement loops) with a different degree of coupling (indicated by the slope of the loops) and different phase difference of the two motions (indicated by the width of the loops). All three blades follow an anti-clockwise rotation (indicated by the symbol in the loops which denotes the starting point on the loop). It is interesting to note that blade 3 essentially undergoes an in-plane motion (flapwise motion) while blade 1 presents the lowest degree of coupling with the flapwise direction.

In Figure 25 & Figure 26, work distributions along the three blades and C_L hysteresis loops (unsteady simulation results) of the three blades at r/R=0.90 are shown for M7 and for the azimuth angles of 20^o and 100^o. For these azimuth angles the work method predicts higher negative work values of the particular mode. In the abovementioned plots 1 m amplitude of the blade tip motion has been considered. Wider hysteresis loops are attained in this way and thereby the unsteady character of the flow is better illustrated. At 20^o rotor azimuth, blade 2 (located at 140^o azimuth) provides the highest negative work. As seen in the C_L-AOA plot blade 2 experiences AOA in the post stall region at negative angles. Negative work is also contributed by blade 1 (located at 20^o). Blade 1 operates in the post stall region at positive AOA. The difference in the shape of the C_L-AOA loops of blade 1 and blade 2 (both lying in the post stall region) is due to the different motions (in terms of flap-edge coupling and phase difference between the two directions of motion) undergone by the two blades in M7 (see Figure 24). Blade's 1 motion is dominated by vibrations in the edgewise direction while blade 2 exhibits a stronger flap-edge coupling. As a result of the higher flapwise component in blade's 2 motion, the range of AOAs seen by blade 2 is also higher. At 100^o rotor azimuth negative work is almost evenly contributed by blades 2 and 3 (located at 220^o and 340^o respectively). Again, the shapes of the C_L-AOA loops of blade 1 on one hand, and blades 2 and 3 on the other, are quite different. This is mainly because of the different flow conditions encountered by the different blades. Blades 2 and 3 operate in deep stall (well within the negative C_L-AOA slope region) while blade 1 encounters light stall conditions (mainly positive slopes up to the C_{Lmin}).

The results of the work analysis agree with those from time domain simulations in turbulent inflow (depicted in Figure 10). In both sets, at the rotor azimuth of 20^o the blade which has an azimuth angle of 20^o is lying in the post stall region at positive AOA, the blade with azimuth angle 140^o is facing stall at negative AOA and the blade with azimuth angle 260^o is also experiencing negative AOA but in the attached flow region. Similarly, for the rotor azimuth of 100^o the blade which is positioned at 100^o angle, is experiencing negative AOA close to C_{Lmin} angle while the other two blades operate in deep stall at negative and positive AOA respectively.

Wind Energ. Sci. Discuss., doi:10.5194/wes-2016-53, 2016
Manuscript under review for journal Wind Energ. Sci.
Published: 23 December 2016

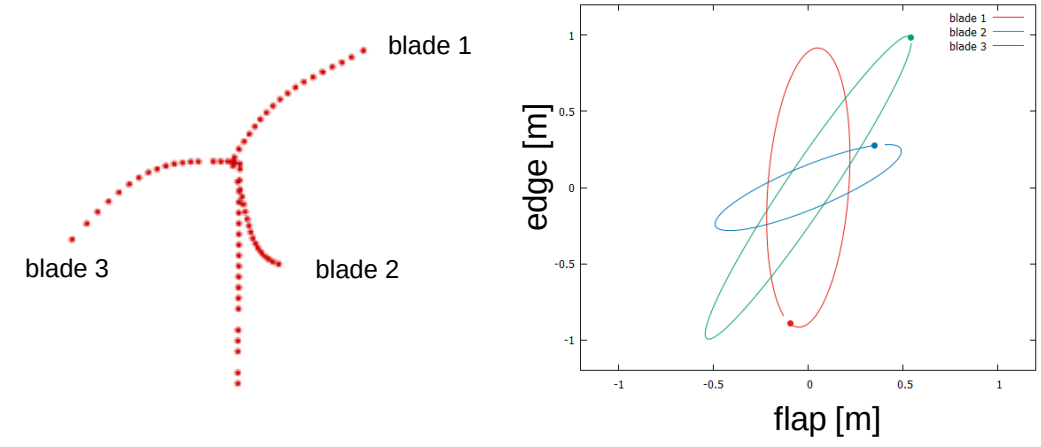

Figure 24. Shape of the lowest damped M7 mode at the azimuth angle of 20°. Trace of the modal displacement of the three blades.

5

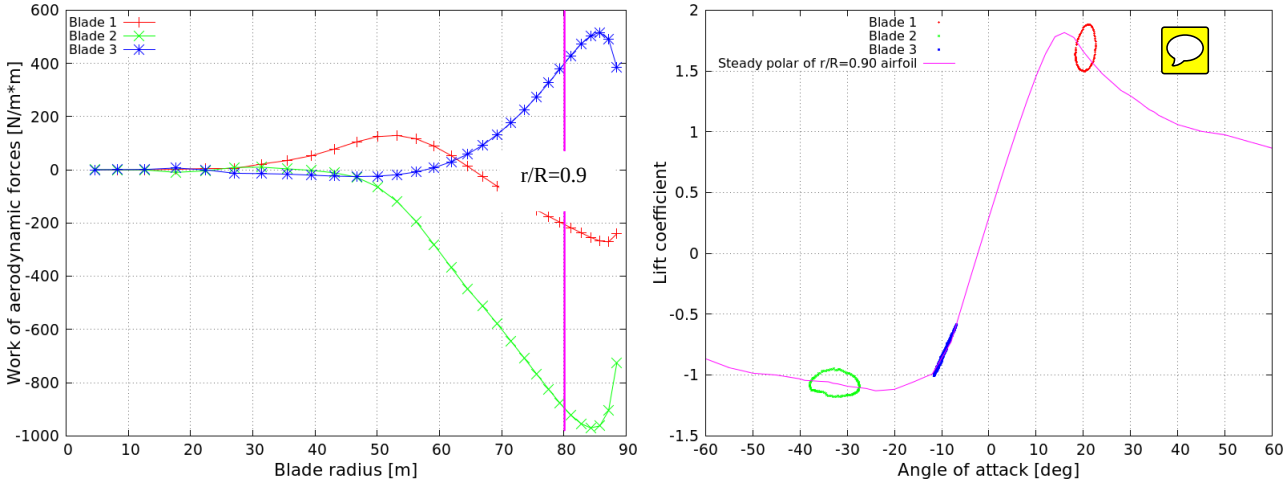

(a) **(b)**

Figure 25. (a) Distribution of aerodynamic work over the three blades for mode M7. Azimuth angle 20°, (b) CL-AOA loops of the three blades at r/R=0.90 for mode M7. Azimuth angle 20°.

Wind Energ. Sci. Discuss., doi:10.5194/wes-2016-53, 2016
Manuscript under review for journal Wind Energ. Sci.
Published: 23 December 2016

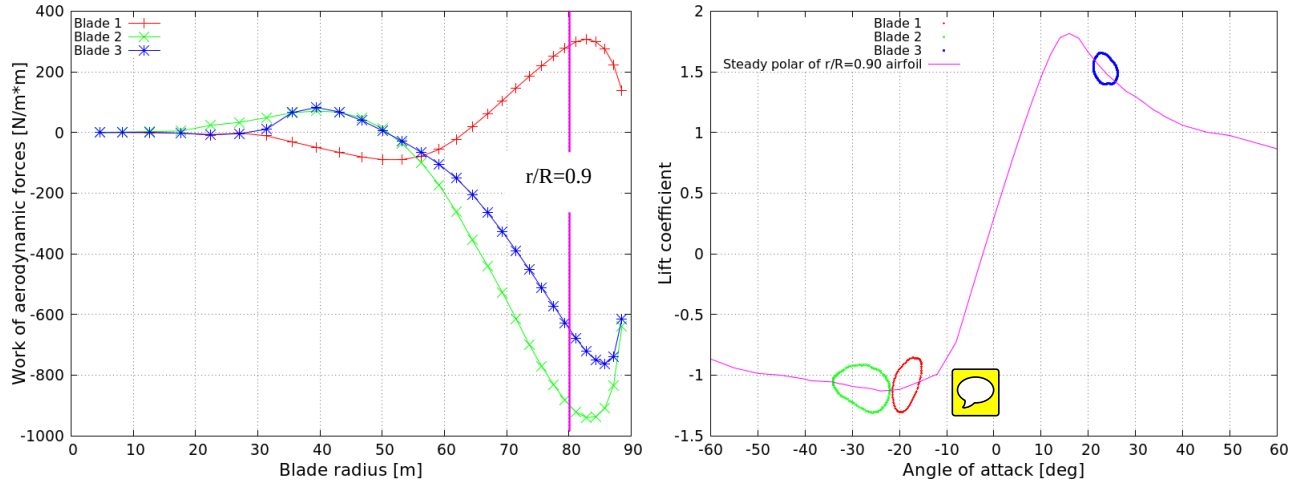

(a) **(b)**

Figure 26. Distribution of aerodynamic work over the three blades for mode M7. Azimuth angle 100°, (b) CL-aoa loops of the three blades at r/R=0.90 for mode M7. Azimuth angle 100°.

5 Conclusions

The aeroelastic stability characteristics of the DTU 10 MW reference wind turbine in standstill or slowly idling operation have been numerically analysed. To this end a consistent and computationally cost effective modelling environment has been presented. It is composed by the core eigenvalue stability analysis tool GAST_lin supported by the non linear time domain aeroelastic analysis code hGAST and a non linear stability analysis tool in which damping is assessed through computations of the aerodynamic work under imposed periodic motion. The predictions of the eigenvalue tool are evaluated through comparisons with the results of both non linear tools. It is a model based validation of the linearized model against its non linear counterparts.

The cross-comparison of the above tools proved that fast linear eigenvalue stability tools can be used as a basis for characterizing stability of turbines in idling operation.

The analysis showed that the lowest damped modes of the 10 MW idling rotor are the out-of-plane ones (symmetric and asymmetric). At yaw misalignment of 30° the asymmetric out-of-plane tilt mode attains negative damping throughout the entire range of azimuth angles. At higher yaw angles stability of the rotor is gradually restored and the damping of the out-of-plane modes returns to positive values. At the yaw angle 30° maximum edgewise loads of the time domain analysis are also obtained. At the above conditions, instabilities are noted in the results of the time domain analysis which through FFT on loads are identified to be linked to the negatively damped out-of-plane tilt mode. Although the instabilities seen in the results of the time domain analysis are not continuously growing as suggested by the negative damping of the eigenvalue predictions they lead to some quite severe stall induced vibrations in the edgewise direction. The less coherent loading conditions developing over the rotor disk under turbulent inflow lead to mitigated vibrations as compared to the uniform

Wind Energ. Sci. Discuss., doi:10.5194/wes-2016-53, 2016
Manuscript under review for journal Wind Energ. Sci.
Published: 23 December 2016

inflow case considered in the stability analysis. As a result of the temporal and spatial variation of the wind the blades are continuously pushed in and out of the negative C_L slope regions and therefore vibrations do not have enough time to build up. At higher yaw angles edgewise loads decrease in agreement with the results of the eigenvalue analysis which predicts positive damping values of the out-of-plane modes at yaw angles higher than 30^o.

Eigen values stability simulations are performed both for steady-state and unsteady aerodynamics. The aim of running simulations also for steady state aerodynamic conditions is to explore the range of damping predictions especially in connection to the fact that many of the state of the art engineering dynamic stall models automatically switch to steady state at very high AOA. Results indicate that steady state analysis is more conservative providing higher negative damping values for all out-of-plane modes.

6 Acknowledgments

The work presented in paper was partially funded from the European Community's Seventh Framework Program under grant agreement No. FP7-ENERGY-2012-1-2STAGE-308974 (INNWIND.EU) and No. FP7-ENERGY-2013-1/no.608396 (AVATAR).

References

Bak, C., Zahle, F., Bitsche, R., Kim, T., Yde, A., Henriksen, L.C., Natarajan, A., Hansen, M.H.,: Description of the DTU 10 MW Reference Wind Turbine, DTU Wind Energy Report-I-0092, 2013.

Bottasso, C., Cacciola, S.: Model independent periodic stability analysis of wind turbines, Wind Energy, 2015, 18(5), pp 865-887

Coleman, R.P., Feingold, A.M.: Theory of self excited mechanical oscillations of helicopter rotors with hinged blades, Technical Report NACA–TN-3844, NACA-TR-1351, Langley Research Center, 1958.

Hansen, M. H.: Improved Modal Dynamics of Wind Turbines to Avoid Stall-Induced Vibrations, Wind Energy, 2003, 6, 179–195.

Hansen, M.H., Gaunaa, M., Madsen, H.A.:A Beddoes-Leishman type dynamic stall model in state-space and indicial formulation, Risoe Report, Risoe-R-1354(EN), 2004.

Hansen, M. H.: Aeroelastic instability problems for wind turbines, Wind Energy, 2007, 10, 551–577.

Heinz, J.C., Sørensen, N.N., Zahle, F., Skrzypiński, W.: Vortex-induced vibrations on a modern wind turbine blade, Wind Energy, 2016, DOI: 10.1002/we.1967

Manolas D.I., Riziotis, V.A., Voutsinas, S.G: Assessing the importance of geometric non-linear effects in the prediction of wind turbine blade loads, Computational and Nonlinear Dynamics Journal, Vol. 10, 041008, July 2015.

Petersen, J.T., Madsen, H.A., Bjorck, A., Enevoldsen, P., Øye, S., Ganander, H. and Winkelaar, D.: Prediction of Dynamic Loads and Induced Vibrations in Stall, Risø–R–1045(EN), Risø National Laboratory, Roskilde, 1998.

Petot, D.: Differential Equation Modelling of Dynamic Stall, Recherché Aerospatiale, 1989, 5, 59–72.

Politis, E.S., Chaviaropoulos, P.K., Riziotis, V.A., Voutsinas, S.G., Romero-Sanz, I.: Stability analysis of parked wind turbine blades, Proceedings of the EWEC 2009, Scientific Track, Marseille, France, March 16-19.

Riziotis, V.A., Voutsinas, S.G., Politis, E.S., Chaviaropoulos, P.K.: Aeroelastic stability of wind turbines: the problem the methods and the issue, Wind Energy, 2004, 7, pp 373-392.

Skrzypiński, W., Gaunaa, M., Sørensen, N., Zahle, F., Heinz, J.: Self-induced vibrations of a DU96-W-180 airfoil in stall, Wind Energy, 2014a, 17 (4), pp 641–655,

Skrzypiński, W., Gaunaa, M., Sørensen, N., Zahle, F., Heinz, J.: Vortex-induced vibrations of a DU96-W-180 airfoil at 90° angle of attack, Wind Energy, 2014b, 17 (10), pp. 1495-1514

Skrzypiński, W., Gaunaa, M.: Wind turbine blade vibration at standstill conditions — the effect of imposing lag on the aerodynamic response of an elastically mounted airfoil, Wind Energy, 2015, 18(3), pp 515–527

Skrzypiński, W., Gaunaa, M., Heinz, J.: Modelling of vortex-induced loading on a single blade installation-setup, The Science of Making Torque from Wind Conference, TORQUE 2016, Munich, Germany, 5-7 October, Journal of Physics: Conference series 753 (2016) 082037.

Skjoldan, P.F., Hansen, M.H.,: On the similarity of the Coleman and Lyapunov - Floquet transformations for modal analysis of bladed rotor structures, Journal of Sound and Vibration, 327, 2009, pp.424–439.

Zou, F., Riziotis, V.A., Voutsinas, S.G, Wang, J.: Analysis of vortex and stall induced vibrations at standstill conditions using a free wake aerodynamic code, Wind Energy, 2015, 18(12), pp 2145-2169.